JGR Solid Earth

RESEARCH ARTICLE
10.1029/2020JB021638

Kinematics of the East Pacific Rise Retrodicted From Pacific and Farallon/Nazca Subduction-Related Torques: Support for Significant Deep Mantle Buoyancy Controlling EPR Spreading

David B. Rowley[1] and **Alessandro M. Forte**[2]

[1]Department of the Geophysical Sciences, The University of Chicago, Chicago, IL, USA, [2]Department of Geological Sciences, University of Florida, Gainesville, FL, USA

Key Points:

- East Pacific Rise (EPR) is not passive
- Subduction related torques do not explain EPR ridge migration history
- Deep mantle buoyancy contributes significantly (∼50%) to plate driving forces through basal tractions

Supporting Information:

Supporting Information may be found in the online version of this article.

Correspondence to:

D. B. Rowley,
drowley@uchicago.edu

Citation:

Rowley, D. B., & Forte, A. M. (2022). Kinematics of the East Pacific Rise retrodicted from Pacific and Farallon/Nazca subduction-related torques: Support for significant deep mantle buoyancy controlling EPR spreading. *Journal of Geophysical Research: Solid Earth*, *127*, e2020JB021638. https://doi.org/10.1029/2020JB021638

Received 26 JAN 2021
Accepted 7 JAN 2022

Author Contributions:

Conceptualization: David B. Rowley, Alessandro M. Forte
Formal analysis: David B. Rowley, Alessandro M. Forte
Methodology: David B. Rowley
Software: David B. Rowley
Validation: David B. Rowley, Alessandro M. Forte
Visualization: David B. Rowley, Alessandro M. Forte
Writing – original draft: David B. Rowley, Alessandro M. Forte
Writing – review & editing: David B. Rowley, Alessandro M. Forte

Abstract Slab-pull together with other boundary-related torques of the Pacific and Farallon/Nazca plates are reconstructed from paleo-agegrid datasets over the past 80 Ma in the no-net rotation (NNR) frame of reference. The resulting reconstructions of both the retrodicted Pacific-Farallon/Nazca age distribution and relative motion history of the East Pacific Rise (EPR) are compared with global plate kinematic reconstructions of these same aspects of Pacific basin evolution. There are mismatches between the predicted and observed age distributions and relative motion history of the EPR. Slab-pull related torques mostly retrodict west to east motion of the EPR, whereas global kinematics result in south to north motions, orthogonal to each other. Slab-pull torques are augmented with estimates of subduction and transform resistances together with spatially variable viscosities to assess their potential contributions to Pacific-Farallon/Nazca relative motions and EPR motions in the NNR frame of reference. We argue that the discrepancies between these different reconstructed histories result from contributions associated with basal tractions acting on the Pacific and Farallon/Nazca plates resulting from deep mantle buoyancy. We propose that the latter has controlled the EPR evolution over the past 80 Ma and significantly contributed to driving plate motions at least in the Pacific basin.

Plain Language Summary We present an analysis of the retrodicted kinematics of the Pacific and Farallon/Nazca plates as a function of time derived from the geometry and age distribution along their plate edges predicated on the predominant view in the tectonics community that slab-pull is the dominant driver of plate motions and accounting for various resistive forces. The retrodicted motions of the East Pacific Rise are orthogonal to the observed motions over the past 45–80 million years. These conflicting motions can be resolved by adding basal tractions, reflecting deep mantle buoyancy beneath the EPR found in a previous study as an approximately equal contributor to slab-pull as the drivers of plate tectonics.

1. Introduction

Plate tectonics has long been considered to be largely driven by slab-pull, the force resulting from negatively buoyant lithosphere at subduction zones, and secondarily by ridge-push, the force resulting from cooling and thickening of oceanic lithosphere (Forsyth & Uyeda, 1975; Richter, 1973a, 1973b, 1977; Solomon et al., 1975). This has led to the view that Earth's convective system is a top-down, plate-driven convective system where the dominant source of buoyancy driving convective flow in the mantle derives from the gravitational potential associated with cooling of plates at the surface and expressed in subduction zones by the sinking of old, cold, dense oceanic lithosphere into the less dense mantle below. Active mantle upwelling in this view is largely limited to hotspots in which relatively narrow plumes of hot mantle rise but do not contribute significantly to the flow driving plates. Otherwise mantle upwelling is viewed as passive, resulting from the divergence of plates at the surface driven by slab-pull and ridge-push.

Within the slab-pull dominated framework, mid-ocean ridges are passive plate boundaries accommodating plate divergence arising from motions driven by far-field forces associated with subducting and cooling oceanic plates. One of the expectations of this interpretation of plate driving forces is that mid-ocean ridges should migrate in a ridge-perpendicular direction at a rate that depends on a combination of factors, namely: plate velocities measured relative to some deep-Earth frame of reference, and half-spreading rate (Stein et al., 1977). Stein et al. (1977) also include spreading asymmetry as a potential geometric contributor, but do not address the drivers of any asymmetric spreading.

Rowley et al. (2016) highlighted that the EPR is characterized by persistent anomalous asymmetry in spreading. On average, ∼44% lithosphere accreted to the Pacific plate, and 56% to the Farallon/Nazca. For simplicity we will refer to this as the Farallon plate, while recognizing that Farallon plate broke up into separate Nazca and Cocos plates about 25 million years ago (Barckhausen et al., 2008), except when referring to the current Nazca plate. On short time and spatial scales, asymmetric accretion appears to dominate, while on longer time and larger spatial scales asymmetric ridge jumps also contribute, at least over the 53 Ma history where ocean floor is preserved on both sides of the EPR (Rowan & Rowley, 2014). Persistent asymmetric spreading is difficult to understand in a plate driven system, since the boundary forces driving plate divergence produce a gap into which asthenospheric mantle passively upwells. On average, this would be expected to accrete symmetrically, as is true of most mid-oceanic ridges. Rowley et al. (2016) account for this persistent asymmetric spreading dynamically, through active coupling of the location of the EPR to a deep mantle upwelling that itself produces asymmetric basal tractions that drag the Nazca plate faster eastwards and the Pacific plate slower westwards relative to the approximately longitudinally fixed upwelling beneath the EPR. The dynamically maintained asymmetric divergence pins the location of the EPR sustaining the observed asymmetric spreading. A passively upwelling system has no similar mechanism to account for this asymmetric spreading.

Rowley et al. (2016) also analyzed ridge residence times that is the integrated time that an actively spreading ridge has occupied any given 0.5 by 0.5 arcdegree grid cell on the surface of the Earth, over the past 83 Ma. Their analysis showed that the East Pacific Rise (EPR) is anomalous relative to most other mid-ocean ridges, being characterized by long ridge residence times despite being Earth's dominant mid-ocean ridge over this time interval. The long ridge residence times of the EPR reflect limited ridge perpendicular motions of this ridge, despite a complex history of subduction along the margins of the Pacific and Farallon and plates derived therefrom.

Within the slab-driven framework, the EPR could be characterized by limited ridge-perpendicular motion if the subduction-related buoyancy and counteracting resistance forces were equal in magnitude and opposite in direction over this time interval. Rowley et al. (2016) analyzed a proxy for the slab-related buoyancy fluxes of the Pacific, and Farallon plates. The buoyancy proxy that they used is the effective subduction zone length times the mean square root of age of subducting plates immediately adjacent to the trench as a function of time. The rationale for this proxy is that slab pull depends on the integrated density difference of the slab relative to the surrounding mantle, that, in turn, depends on the length of the trench along the surface, down-dip length of the subduction zone, slab thickness, and mean density of the oceanic lithosphere. Since slab thickness and down dip length are both small relative to trench length, trench length dominates. Mean density of the oceanic lithosphere increases with square root age hence the second term in the proxy. This aspect of the analysis showed that this proxy is significantly different for the Pacific and Farallon plates, independent of plate area. Hence, they argued that limited ridge perpendicular migration of the EPR is not compatible with a balancing of the subduction buoyancy fluxes on either side of the EPR.

Rowley et al. (2016) thus argued based on their kinematic and geodynamic interpretations of EPR stability that the traditional plate driving force framework predicated on the dominance of slab-pull was incorrect. A major conclusion of their study is that mantle-convection-driven basal shear stresses acting below tectonic plates is a major contributor to plate motions, in particular in the Pacific Ocean. This conclusion is supported by a number of earlier mantle flow studies focusing on the dynamical origins of observed plate motions, notably involving tomography-based models in which basal shear tractions drive predicted plate velocities that closely fit observations (e.g., Becker & O'Connell, 2001; Forte, 2011; Forte et al., 2009; Ghosh & Holt, 2012; Ricard & Vigny 1989). The importance of basal shear stresses in explaining observed plate motions was also considered in finite-element models of the lithosphere that incorporate complex rheology and fault structures (Bird et al., 2008). More recent modeling of Pacific plate driving forces by Stotz et al. (2018) similarly suggests a strong contribution from basal shear tractions due to depth-dependent increases of horizontal flow in the asthenosphere.

Rowley et al. (2016) presented a geodynamical model showing that an elongated, ridge-parallel curtain of actively upwelling mantle controls EPR kinematics and dynamics, over at least the past 80 Ma. Importantly, this model also shows asymmetry in the divergence field beneath the EPR matching the observed asymmetry recorded by plate accretion. In this model (see also Glišović & Forte, 2014) the upwelling mantle beneath the EPR spreads laterally within the asthenosphere, with flow velocities that are faster than the surface plates. These authors thus argued that basal shear tractions related to this flow significantly contributed (∼50%) to plate motions, at least in the Pacific region. This suggestion is not unreasonable given recent estimates that up to 50% of the heat flux at the top of the mantle may be extracted from the core (de Koker et al., 2012; Pozzo et al., 2012), thus sustaining large-scale hot mantle upwellings contributing to mantle convection (Glišović et al., 2012). As shown by Forte (2011), Rowley et al. (2016) these flows are organized as part of the large-scale mantle flow field that includes the plates themselves and thereby contributes directly in driving plate tectonics.

Various approaches have been followed to quantify plate driving forces since the classical treatments of Richter (1973a, 1973b, 1977) and Forsyth and Uyeda (1975). For example, Becker and O'Connell (2001) parameterized an array of plate driving forces and edge forces (as in Forsyth & Uyeda, 1975) that include slab-pull, collision resistance, ridge-push, transform resistance, thickness variations of the lithosphere from plate cooling, with and without inclusion of contributions from continental topography, among others. As expected, when they considered only lithosphere and resisting plate-edge forces (using a-priori estimates for the latter), slab-pull dominated. The correlations between predicted and observed present-day plate motions improved when they included deeper mantle flow induced by estimates of slabs within the whole mantle.

Subsequently, Bird et al. (2008) used a finite element model of the lithosphere (Bird, 1999) to estimate plate driving forces. They consider the classical forces, including all of those listed above, as well as basal tractions. They point out that the majority of plates have little or no attached subducting slabs and thus are not well matched to the classical analyses. Their primary conclusion is that basal tractions operating in the direction of plate motion are important, particularly for what they refer to as slabless plates. An important caveat is that their analysis did not explicitly separate basal tractions from net slab-pull in the assessment of subducting plates. For these plates, the effect of basal tractions was included in their "net slab-pull" term, the difference between slab-pull and subduction resistance, with no basal tractions on these plates. Other than ascribing basal tractions as related to "deep" mantle convection, they do not explicitly address the source of those tractions.

In contrast, Ghosh and Holt (2012) explicitly included the contributions of basal tractions in modeling present-day plate motions with forces arising from both lithospheric and sublithospheric sources, where the latter were predicted using buoyancy forces derived from a global seismic tomography model. They found a best match that included mantle flow, mostly acting as a driving force but locally resisting plate motions.

The negative buoyancy associated with subduction of oceanic lithosphere expresses itself through the generation of torques acting on the plates thereby contributing to their motions (Solomon et al., 1975; Solomon & Sleep, 1974). One potential criticism of the subduction buoyancy proxy presented by Rowley et al. (2016) for slab-pull driven plate motions is that it did not explicitly treat plate-driving torques. The buoyancy flux proxy of Rowley et al. (2016) thus needs to be converted to the corresponding torques acting on the Pacific and Farallon plates to correctly demonstrate that the observed absence of ridge-perpendicular motion is not a consequence of the far-field action of the subduction-related torques acting on these plates along the EPR.

In this study, we re-examine the classical modeling of plate driving forces by considering two subducting oceanic plates in the Pacific Ocean as a function of time. This will permit an exploration of their explanatory power relative to observed motions of these plates and their common plate boundary, the East Pacific Rise. We will thus present a new assessment of subduction-related torques as a function of time and consider their implications for EPR kinematics. The results are intuitively obvious given the basic geometry of the western Pacific and America's subduction zones. To first-order, these subduction zones lie along the west and east sides of the subducting plates, yielding torques and corresponding rotations near the south and north poles, respectively. The resulting retrodicted plate motions are to the west and east, with the retrodicted motion of the EPR also from west to east, orthogonal to the motions of the EPR in the no-net-rotation (NNR) and other mantle frames of reference (Rowley et al., 2016).

2. Slab-Pull Induced Torques and Plate Rotations

The 'slab-pull' force per unit length acting along subducting plate boundaries due to the negative buoyancy of descending oceanic slab is given by Turcotte and Schubert (2002) (Equation 6.388) as

$$F_S(t) = 2\Delta\rho g d\sqrt{\frac{\kappa t}{2\pi}}, \quad \Delta\rho = \rho_0\alpha(T_c - T_0) \tag{1}$$

where t is age of the subducted lithospheric material, κ is the thermal diffusivity ($\approx$1 mm^2/s = 10^{-6} m^2/s), α is the volume coefficient of thermal expansion ($\approx 3 \times 10^{-5}$ K^{-1}), ρ_0 is the average density of the lithosphere (3,300 kg/m^3) at ambient surface temperature, $\Delta T = T_c - T_0$ is the temperature difference between the surface and the adiabatic interior of the convecting mantle ($\Delta T \approx 1200$ K), and g is the average gravitational acceleration ($\approx$10 m/s^2).

The depth of penetration of the subducting slab, d, will be assumed a constant, equal to 700 km. Maximum depths of the dominant slabs of the Nazca and Pacific system of >620 km (Hayes et al., 2018) are in reasonable accord with this assumption. The assumption that all slabs descend to the top of the lower mantle is a simplification that has also been invoked in previous modeling of slab pull forces (e.g., Faccenna et al., 2012). This simplification can be relaxed, if needed, in subsequent analyses. Employing the ages of subducted lithosphere over the past 80 Ma from the Müller et al. (2008) plate reconstructions, the mean value of $\sqrt{t}$ (averaged over the total length of the subduction zone, where t is expressed in Ma) varies from ∼5.4 to ∼8 for the Pacific plate and from ∼5.4 to ∼7.6 for the Farallon plates. In our use of expression (1) below, we explicitly integrate the local varations of $\sqrt{t}$ along all subduction zones. We can readily estimate the approximate magnitude of the slab pull force by employing $\sqrt{t} = 7.75$ (mean subduction age = 60 Ma) in expression (1), using the physical parameter values described above, to obtain a value of $F_S \simeq 2.4 \times 10^{13}\, N/m$.

We assume negligible conductive heating of slabs as they descend across the upper mantle, which is valid for a high Peclet number. In most of our models we include an effective reduction of the slab pull force in (1) arising from opposing dissipative stresses in the mantle and lithosphere (e.g., plate bending Buffett & Rowley, 2006; Conrad & Hager, 1999) that act to reduce the total force the slab transmits to the edge of the subducting plate. Following Stotz et al. (2018), we explored slab-pull reduction factors ranging from 25% to 75%.

An evaluation of expression (1) yields the slab-pull force per unit length parallel to the strike of the trench. Following Solomon and Sleep (1974), Solomon et al. (1975), and derivations presented in the Appendix A the total torque $\vec{\tau_S}$ due to the slab-pull force acting on a subducting plate is given by the following path integral:

$$\vec{\tau_S} = r_0 \int F_S(t)\, \vec{dl} \tag{2}$$

where r_0 is the radius of Earth's solid surface and $\vec{dl}$ is an infinitesimal vector displacement along the plate perimeter, proceeding counterclockwise relative to the plate interior.

The slab-pull torque (2) will drive a rotational motion of the plate that will be opposed by drag-related viscous tractions acting on the base of the plate (Figure A1). Assuming an otherwise static asthenosphere, the viscous torque, $\vec{\tau_V}$, generated by these basal tractions (see Appendix A for details) may be mathematically expressed as follows:

$$\vec{\tau_V} = -D r_0{}^2 A \hat{e}_i [\delta_{ij} - \widehat{S_{ij}}]\omega_j, \quad \text{where } \widehat{S_{ij}} = \frac{1}{r_0^2 A} \iint_A x_i x_j \, dA, \tag{3}$$

which involves a drag coefficient $D = \eta/h$, the ratio of viscosity η to depth h of the Couette shearing flow (Figure A1), the Cartesian components ω_i of the plate rotation-rate vector, the total plate area A, and the position vector $\vec{r} = \hat{e}_i x_i$ is defined with respect to Earth's center of mass. In most applications h is assumed to correspond to the depth of the asthenosphere, or the low-viscosity region below the plates, which accommodates the shear associated with plate motions. The use of a constant (i.e., spatially uniform) value of the drag coefficient D yields plate motions in a NNR mantle frame of reference (Solomon & Sleep, 1974).

In addition to viscous basal drag, there are resistive or frictional forces acting on the edges of the plate. A number of opposing edge forces have been considered in past analyses, such as collisional resistance, transform resistance and slab resistance (e.g., Forsyth & Uyeda, 1975). Past assessments of the importance of these resistive edge forces relative to slab pull reveals large non-uniqueness (Becker & O'Connell, 2001; Forte, 2011 for a review). The outstanding challenge is the difficulty in estimating realistic magnitudes for these edge forces, due to the considerable uncertainty in determining appropriate values for the physical parameters needed to model the complex rheology of the lithosphere and crust and the stress state in plate-boundary fault zones (e.g., Bird et al., 2008; Takeuchi & Fialko, 2012). In the following treatment, we will include two potentially important resistive forces that act on plate boundary edges, namely the collision resistance at subduction zones and resistance acting parallel to transform faults.

Employing the formulation in Becker and O'Connell (2001), we mathematically represent the torques generated by these resistive forces as follows (see Appendix A for further details):

$$\text{(transform resistance)} \quad \vec{\tau_T} = -C_T \; r_0 \int_{TF} sgn(v_t) \; \hat{r} \times \hat{l} \;\; dl, \tag{4}$$

$$\text{(collision resistance)} \quad \vec{\tau_C} = -C_C \; r_0 \int_{CR} \hat{r} \times \hat{n} \;\; dl, \tag{5}$$

where $\hat{r}$, $\hat{n}$, $\hat{l}$ are the unit radial, normal, and tangential vectors (defined relative to the local strike of the plate boundary), respectively (see Equation A2), and $sgn(v_t) = 1$ or -1, depending on the orientation of the tangential relative velocity, v_t, with respect to the tangent vector $\hat{l}$. The factors C_T and C_C determine the local magnitude or strength of the transform and collision resistance forces. In Becker and O'Connell (2001) the values assumed for these constants are: $C_T = C_C = 2 \times 10^{12} \;\; \mathrm{N/m}$, which correspond to an average resistive force magnitude of 20 MPa acting on the edge of a 100 km-thick lithospheric plate. Here we again assume that $C_C = 2 \times 10^{12} \;\; \mathrm{N/m}$, a value that has also been inferred by Bird et al. (2008), but we will explore values for the transform resistance forces that are different. The finite-element stress models of Bird et al. (2008) suggests strong reductions in fault friction coefficients for the lithosphere, which imply transform resistance may be substantially smaller than collision resistance: $C_T \ll 2 \times 10^{12} \;\; \mathrm{N/m}$. For several of the experiments described below we therefore adopt a value of $C_T = 2 \times 10^{11} \;\; \mathrm{N/m}$.

Because of the extremely high effective viscosity of the mantle, the deformation associated with plate-tectonic movements is quasistatic and inertia is negligible, thus implying that the sum of all torques acting on each tectonic plate must be zero:

$$\vec{\tau_S} + \vec{\tau_T} + \vec{\tau_C} + \vec{\tau_V} = 0. \tag{6}$$

Substitution of Equations 2 to 5 into 6 yields the following system of linear equations (see Appendix A for details) for the instantaneous angular velocity vector, $\vec{\omega}$, of each plate:

$$\omega_i = (Dr_0A)^{-1} A_{ij}{}^{-1} \;\; \hat{e}_j \cdot \left[\int_{SP} F_S(t) \, \vec{dl} - C_T \int_{TF} sgn(v_t) \;\; \hat{r} \times \vec{dl} - C_C \int_{CR} \vec{dl} \right] \tag{7}$$

where summation over all values of j is implied. The symmetric matrix A_{ij} (see Equation 3) depends on the plate geometry only and is analogous to a moment of inertia tensor:

$$A_{ij} = [\delta_{ij} - \widehat{S_{ij}}], \tag{8}$$

where all terms are defined in (3).

As is evident in (7), the magnitude of predicted plate rotation-rates is inversely proportional to the drag coefficient $D = \eta / h$, where η is viscosity and h is the depth of the deforming layer, usually taken equal to the asthenosphere. A-priori estimates of this coefficient may be obtained from independent geodynamic constraints on mantle viscosity and asthenospheric thickness, as in Stotz et al. (2018). These authors infer a range of values for both η and h that imply corresponding variations for D that range from $\sim 2 \times 10^{14} \;\; \mathrm{Pa \;\; s/m}$ to $\sim 4 \times 10^{15} \;\; \mathrm{Pa \;\; s/m}$. Constraints on horizontally averaged upper-mantle viscosity from joint inversions of glacial isostatic adjustment (GIA) and mantle convection data sets (Forte et al., 2010; Mitrovica & Forte, 2004) yield an average viscosity from 100 to 400 km depth of $\eta = 2.4 \times 10^{20} \;\; \mathrm{Pa \;\; s}$. If the deformation due to plate-driven (Couette) viscous flow is Approach 1 rotates the template $\approx 8 \times 10^{14} \; \mathrm{Pa \;\; s/m}$, which is in the mid-range of estimates implied by the analysis of Stotz et al. (2018). There is a non-negligible uncertainty in such estimates of the drag coefficient, owing to the uncertainties in current inferences of mantle viscosity and uncertain trade-offs with the depth interval over which most of the plate-driven mantle deformation would occur. Moreover, the horizontal-average viscosity below different plates may vary significantly, thus implying corresponding lateral variations of the drag coefficient. With these

Table 1
Model Parameters for Plate Torque and Rotation Calculations

Model	Naz SP[a]	Pac SP[a]	CR[b]	TF[b]	Naz D[c]	Pac D[c]	h[d]	η_a[e]
1	1.	1.	0.	0.	2.0	2.0	120	6.
2	1.	1.	2.	2.	1.7	1.7	141	5.1
3	1.	1.	10.	2.	0.96	0.96	250	2.9
4	0.75	0.25	2.	1.	2.2	0.18	109, 1,333	6.6, 0.54
5	0.5	0.5	2.	0.2	0.81	0.81	296	2.4
6	0.25	0.25	2.	0.2	0.30	0.30	800	0.9
7	0.25	0.45	2.	0.2	0.39	0.65	615, 369	1.2, 1.9
8	0.5	0.5	2.	0.2	0.77	0.77	311	2.3

[a]slab-pull reduction factor, $f \leq 1$, where weight of slab is reduced by this factor. [b]magnitude, C, of collision resistance (CR) or transform fault (TF) resistance, in units of $10^{12}\ \ N/m$. [c]Inferred drag coefficient, in units of $10^{15}\ \ Pa\ \ s/m$, that maximizes fit to recent plate motions. [d]Depth of Couette flow, in units of km, coupled to plate motions, assuming asthenospheric viscosity $\eta_a = \ 2.4 \times 10^{20}\ \ Pa\ \ s$ (Forte et al., 2010; Mitrovica & Forte, 2004). When two values are given, they refer to the Naz and Pac plates respectively. [e]Inferred asthenospheric viscosity η_a, in units of $10^{20}\ \ Pa\ \ s$, assuming depth of Couette flow $h = 300\ \ km$. When two values are given, they refer to the Naz and Pac plates respectively.

uncertainties in mind, in the next section we will employ time-dependent surface plate kinematics as an independent constraint on the drag coefficient and evaluate its compatibility with the a-priori estimates discussed here.

3. Data and Results

In the following, we employ expression (7) to derive the set of rotations for the Pacific and Farallon plates that correspond to balancing the slab-pull and opposing resistive forces acting on these plates as a function of time. These rotations then allow for the reconstruction of the East Pacific Rise in the NNR frame of reference, where EPR motions are entirely determined by the balance of torques acting on the Pacific and Farallon plates.

Following Rowley et al. (2016) we use the paleo-plate age grids of Müller et al. (2008) and corresponding plate polygons (Gurnis et al., 2012) to determine the age (t) and trench element length (dl) along trenches bounding the Pacific and Farallon plates as a function of time from 80 Ma to the Present. We then integrate counter-clockwise along each boundary following Equation 7 to derive the resulting slab-pull related torque, which, in most of our models, includes resistive forces acting on plate edges. We further combine paleo-plate age grids and instantaneous rotations derived from Seton et al. (2012) to algorithmically identify segments of the plate polygons acting as transform faults using an angle of ≤25° between the boundary orientation and the relative plate motion velocity vector. Along the identified transform boundaries, we compute the transform resistance using Equation 4.

In the following section, we explore eight models incorporating slab-pull with various estimates of the resistive forces. These models and their input parameters are summarized in Table 1. For each scenario we provide corresponding estimates of the slab-pull related torques of the Pacific plate as a function of time in Table A1. Table A2 presents the slab-pull related torques of the Farallon plate as a function of time. Table A3 presents the instantaneous torque rotations of the Pacific to NNR and Farallon to NNR as a function of time for each of the models. Table A4 lists finite rotations of the Pacific to NNR and Farallon to NNR as a function of time for each of the models. Table A5 of the Farallon plate relative to the Pacific plate for each of the models. We underline that for the first seven models, the value of D is optimized to match recent plate motions. This is further discussed below.

The first model uses only ($\vec{\tau_S}$) and viscous drag (τ_V) that corresponds with traditional views of a pure slab pull-driven system. Model 2 includes all boundary forces, meaning $\vec{\tau_S} + \vec{\tau_T} + \vec{\tau_C} + \vec{\tau_V}$, with values of the coefficients in Table 1. The third model is $\vec{\tau_S} + \vec{\tau_T} + 5\ \vec{\tau_C} + \vec{\tau_V}$, significantly enhancing the subduction and collision resistances. In model 4, slab pull is scaled by 0.75 $\vec{\tau_S}$ for the Farallon plate and 0.25 $\vec{\tau_S}$ for the Pacific plate, while the transform resistance is one half the collision resistance (Table 1). Another key feature of model 4 is that the drag coefficients below the Pacific and Farallon plates are allowed to differ to further optimize the fit to 0 Ma plate motions. In model 5, slab pull is reduced by 50% and the drag coefficient is the same for both plates, but transform resistance is 10 times smaller than collision resistance and this applies to all subsequent models 6–8

(Table 1). Similarly, in model 6, slab pull is scaled to 25% while including other resistive forces. Model 7 applies both different reductions in the slab pull coefficients, by 0.25 $\vec{\tau_S}$ for the Farallon plate and 0.45 $\vec{\tau_S}$ for the Pacific plate, and different drag coefficients ($\vec{\tau_V}$) under the Farallon and Pacific plates. In each of the above, the value of D is optimized to match some estimate of recent plate motions, as discussed below. Finally model 8, uses an a priori value of D based on both an estimate of asthenospheric viscosity from Mitrovica and Forte (2004) and thickness of the deforming layer (300 km). In order to match recent plate motions, but, without rescaling of D, the best match is achieved when the slab pull force on both the Farallon and Pacific plates is reduced to 50%. In this sense, we treat D as a free variable in the analyses of results of models 1 through 7.

As discussed in the preceding section, we may independently estimate the drag coefficient $\boldsymbol{D}$ such that its value optimizes the match with short-term relative motion of Nazca to Pacific plates derived from marine magnetic reversal data. In this exercise, the optimization is based on fitting to rotations derived by Seton et al. (2012) and Torsvik et al. (2019) that underlie the agegrid reconstructions (Müller et al., 2008) that combine poles for Nazca to Antarctica (Tebbens & Cande, 1997) with Pacific to Antarctica (Croon et al., 2008) to derive a 5.0 Ma rotation of Nazca to Pacific. These optimized drag coefficients along with their corresponding depth of deformation and viscosity values are summarized in Table 1.

It is important to note that this approach to the derivation of D maximizes the fit of the model to the observed plate motions integrated over the past 5 Ma. In this sense, D effectively trades off with slab-pull and various resistance forces, particularly collision/subduction resistance and transform resistance. For example, if only slab-pull forces are considered, models with $\vec{\tau_S}$ and 0.25 $\vec{\tau_S}$ yield identical results, because differences in D precisely cancel any difference. Similarly, comparing models 5 and 6 (Figures 1f and 1g) that despite a factor of 2 difference in the fractional slab pull from 0.5 to 0.25 there is not much difference in the retrodicted isochrons. This reflects that optimizing D changes its value by a bit more than a factor of 2 to match observed plate motions largely compensating for the change in slab pull. This has the consequence of improving the fits of retrodicted isochrons relative to models in which D is not adjusted. Values of D are listed in Table 1 for each of the models. Also included are values of h and asthenospheric viscosity, assuming either a fixed asthenopheric viscosity to compute depth (h), or fixed depth (h) to compute viscosity that would be implied by these values of D. The models themselves only use values of D, these other columns are for comparison purposes only.

In order to visualize the implications of these calculations we generate a set of synthetic isochrons for the EPR between the Galapagos and Easter triple junctions using simplified 1MY isochrons on the Pacific Plate derived from the Müller et al. (2008) age grid as templates (Figure 1a). Isochrons on the Pacific plate are rotated onto the Nazca plate using rotations in Rowan and Rowley (2014), and Cocos, and Antarctic plates using rotations in Rowan and Rowley (2016), Rowley et al. (2016). We treat the combined set of isochrons on the Nazca and Pacific plates generated along the EPR between the Galapagos and Easter triple junctions as the observed/model data that we use as our comparison set. The same set of isochron templates are also used to generate synthetic isochrons on the Farallon plate based on the various model parameters listed in Table 1. It is worth noting that the asymmetry in spreading along the EPR can only be explicitly quantified up to chron 23R (~51 Ma), the oldest marine magnetic anomaly identified on the Nazca plate (Cande & Haxby, 1991). The degree of asymmetry varies spatially and as a function of time but averages about 44% accreting to the Pacific plate and 56% to the Nazca plate over the past ~51 Ma (Rowan & Rowley, 2014).

For times older than 51 Ma, we do not know how much or whether asymmetric spreading persisted along this boundary. For the isochrons shown in Figure 1a we assume that the degree of asymmetry was unchanging to at least 80 Ma. A second point worth noting is that for ages older than 51 Ma rotations of Farallon to Pacific are derived by summing so-called half-angle rotations by determining best fitting rotations of data on the Pacific plate alone. For example, magnetic anomaly picks of chron 24old (~53 Ma) are rotated onto picks of chron 20old (~44 Ma). This "half"-angle rotation is multiplied by either 2, assuming symmetric spreading or in our case 2.273, to account for the average asymmetry of spreading. If we were to assume that asymmetric spreading did not persist beyond 51 Ma then the finite rotations of Farallon to Pacific would be correspondingly reduced and the observed/modeled isochrons for ages older than 51 Ma would not project as farther to the east on the Farallon plate (Figure 1a). Thus, when comparing torque-derived predicted results with observed/model isochrons we have used a kinematic model that reconstructs isochrons farther east than would be the case for no further asymmetric spreading, thereby expanding the areal extant of the isochrons and decreasing the misfit relative to the majority of model experiments that we consider below.

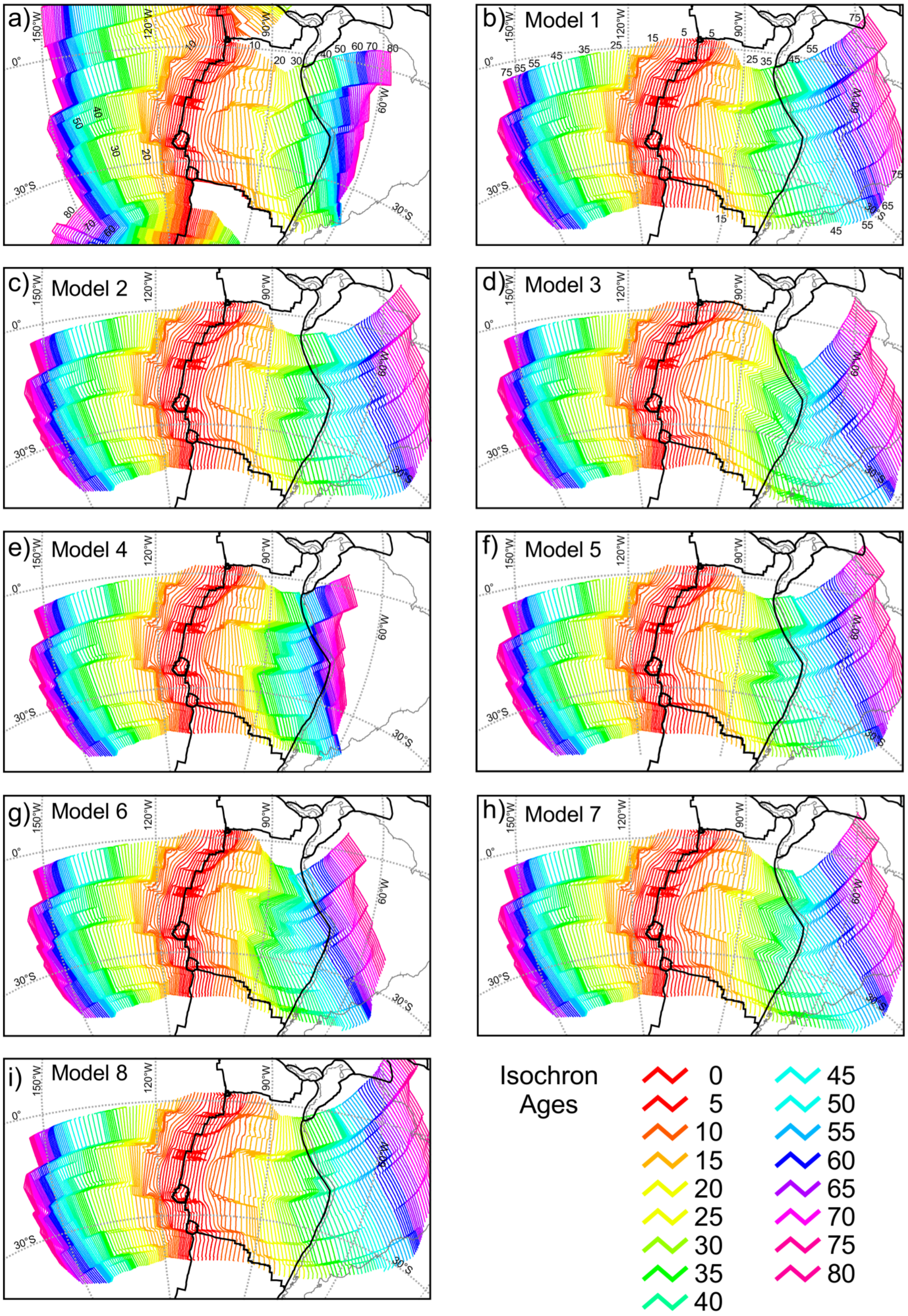

Figure 1. Lambert equal area projections of simplified isochron geometries in the Pacific, where modern ridges are from Rowley (2018) and other plate boundaries are from Bird (2003). (a) Simplified Pacific isochrons with 1 MY spacing from Müller et al. (2008) together with modeled reconstructed Nazca and Cocos isochrons rigidly attached and projected at the surface of the subducted plates. Rainbow colors from 0 (red) to 80 (purple) Ma. (b) through (i) Isochron locations retrodicted by Pacific and Farallon modeled plate torque histories for each of the 8 models described in the text using approach 1.

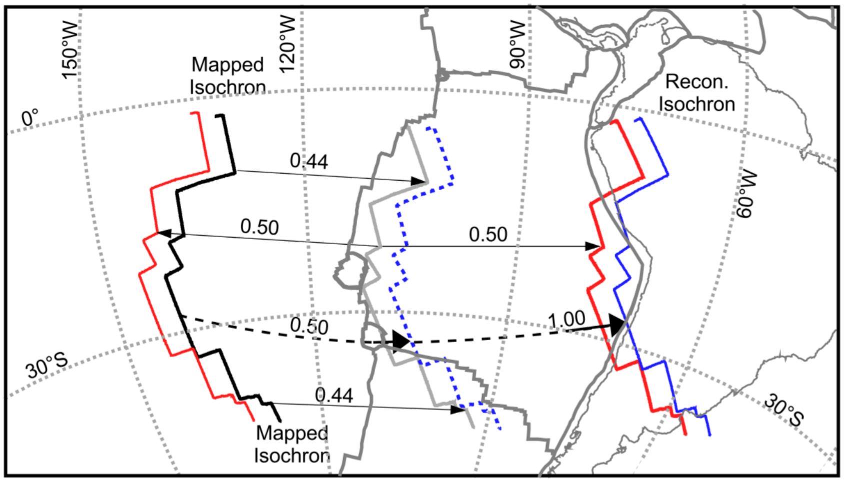

Figure 2. Lambert equal area projection of mapped 40 Ma Pacific isochron as a template (black) and the two approaches used to create synthetic isochrons based on the torque-derived models. Approach 1 rotates the template by 0.44* model 40 Ma rotation to approximately place the template over the current EPR (gray), followed by ±05* model 40 Ma rotation to produce synthetic isochrons on the Farallon and Pacific plates (red). Approach 2 holds the 40 Ma Pacific isochron fixed and creates the conjugate Farallon using the full 40 Ma model rotation (blue) with an implied EPR location shown by the dashed blue template.

Along most mid-oceanic ridges, the generation of synthetic isochrons is straightforward. A template of a given isochron is placed at the ridge axis, using a half-angle rotation and projected onto each plate by half-angle rotations. Equivalently, a template from one plate is simply rotated onto the adjacent plate using the full rotation. The Pacific-Farallon EPR does not conform with this model because of the persistent asymmetric spreading. Figure 2 shows the two approaches that we use to reconstruct synthetic isochrons along this segment of the EPR. In this example, the mapped 40 Ma Pacific isochron (black) is the template. Since one component of this analysis focuses on the motion of the EPR in the NNR frame of reference, it seems appropriate to place the template close to the EPR (gray) by scaling the full rotation by 0.44, rather than farther to the east as would result from applying a half angle rotation (dashed blue). Approach 1 uses the gray template that is then rotated by half-angle rotations onto both the Pacific and Farallon plates (red) under the assumption that because plate driving forces act far from the ridge axis, that plate divergence generates a gap into which asthenospheric mantle passively upwells (Elsasser, 1971; Parsons & Richter, 1980) such that spreading is expected to be symmetric. For many of the models this approach minimizes misfits with the observed/modeled Pacific- Farallon isochrons, by distributing misfit to both the Pacific and Farallon plates (Tables 2 and 3). Alternatively, approach 2 simply rotates the Pacific isochron onto the Farallon plate using the full rotation (solid blue), as would be appropriate for a symmetrically spreading ridge. This forces all misfit of observed with modeled age distributions onto the Farallon plate. Implicit in approach 2 is that the implied passively upwelling ridge (blue dashes) would be significantly displaced relative to the EPR. However, because the reconstruction of EPR motion relative to NNR is based on the reconstructed synthetic isochrons and not the implied symmetric ridge, approach 2 implicitly embeds the asymmetric spreading history of the EPR without actually explaining or accounting for it. For many models this approach significantly increases the misfit of Farallon isochrons by further accentuating the asymmetry of Farallon motions (Tables 2 and 3).

Finite rotations are integrals of instantaneous rotations calculated from the plate torques. The resulting isochrons are by construction similar to observed isochrons at young ages because at relatively small rotation angles (~30°) the differences are not great so long as the torque-derived poles are within ~30° of the kinematically determined finite rotation pole. As a result, differences mostly become apparent at older (>~45 MY) ages and by mismatches of the areal distributions of observed and modeled ages. Several metrics can be used to compare torque-derived and kinematic-derived age distributions. For example, the oldest oceanic lithosphere currently in the Peru-Chile Trench, identified by magnetic anomalies, is ~51 Ma at latitudes of ~18°S and 22°S (Cande & Haxby, 1991). Farther south at ~32°S the age of oceanic lithosphere within the trench is ~40 Ma (Cande & Haxby, 1991). We have chosen six sites within or immediately adjacent to the Peru-Chile Trench where Cande and Haxby (1991) have identified magnetic reversals. These can be compared with each of the torque-derived reconstructed isochron ages

Table 2
Comparison of Observed Trench Ages With Model Predictions

Long.	Lat.	Chron	Age	1	2	3	4	5	6	7	8
Symmetric spreading about EPR											
−73.32	−18.07	23	51	46	45	41.5	64	46	46	60	41.5
−71.41	−21.99	23	51	47	44	47	68	45	46	57	42.5
−71.52	−25.00	21R	48	44.5	45	45	63	45	44	57	40.5
−72.56	−32.22	18	40	39	39	40.5	50	39	39	47	34.5
−72.76	−33.83	17	38	38	38	39	48	38	38	46	32.5
−74.12	−36.16	13	34	33.5	33.5	35	43	33	35	43.5	29
			% Error	28.9	35.7	39.5	167.9	33.3	33.4	114.7	93.8
Asymmetric spreading about EPR with fixed pacific isochrons											
−73.32	−18.07	23	51	42.2	39.6	73.8	54.5	40.5	41	54.8	36
−71.41	−21.99	23	51	43	40.8	69.3	56.5	41.5	40.5	52	39
−71.52	−25.00	21R	48	41.2	41.2	68	54	41.5	39	51	37
−72.56	−32.22	18	40	35.9	35.8	64.1	46	36	36	44.8	32
−72.76	−33.83	17	38	34.8	34.6	62	41	34.5	34.5	43.2	29.5
−74.12	−36.16	13	34	30	30.5	58.4	38	30	32	40.8	26.4
			% Error	77.5	86.3	317.4	64.8	83.7	84.0	61.3	140.6

Note. Ages are in MY.

at those locations. These comparisons are listed in Table 2. For the oldest oceanic lithosphere in the Peru-Chile trench the age differences are generally >5 million years. We quantify the misfit using the percent error, for each of the models and both of the approaches used to reconstruct the Pacific and Farallon synthetic isochrons. The percent error ranges from 28.9% for model 1 and approach 1%–317.4% for model 3 and approach 2. Models 2,

Table 3
Correlation Coefficients and Percent Error of Age Distributions of Modeled Isochrons Versus Observed/Kinematically Reconstructed Ages for Both Approaches 1 and 2

Models	1	2	3	4	5	6	7	8
Approach 1								
Overlap	79%	76%	70%	87%	77%	74%	84%	78%
Nonoverlap with observed	2%	2%	4%	6%	2%	3%	3%	3%
Nonoverlap with predicted	19%	22%	26%	7%	21%	23%	14%	18%
Total area R	0.145	0.085	0.061	0.246	0.135	0.121	0.312	0.074
% Error	66.4	75.1	89.5	56.8	70.4	77.0	60.0	62.7
Pacific R	0.202	0.198	0.207	0.311	0.203	0.207	0.279	0.179
% Error	60.3	60.1	57.1	49.5	59.7	58.3	51.4	64.0
Farallon R	0.135	0.044	−0.002	0.197	0.117	0.093	0.340	0.033
% Error	72.2	89.3	120.3	63.8	80.6	94.7	68.2	61.4
Approach 2								
Overlap	74%	69%	55%	90%	71%	66%	78%	75%
Nonoverlap with observed	2%	2%	11%	6%	2%	3%	2%	4%
Nonoverlap with predicted	24%	29%	34%	5%	27%	31%	19%	21%
Farallon R	−0.030	−0.116	−0.173	0.573	−0.055	−0.095	0.321	−0.103
% Error	80.5	100.5	201.9	31.8	90.7	107.6	75.2	70.1

3, 5, and 6 yield reasonably comparable errors for approach 1, whereas models 4 and 7 yield the lowest percent errors based on approach 2, albeit with double the percent error to approach 1.

Another approach to quantifying the torque-derived reconstructed age distributions is to compute the total percent error and associated correlation coefficient with respect to the observed/kinematic model-derived age distribution that are presented in Table 3. Correlation coefficients and percent error are calculated by comparison of 0.1 arcdegree grids derived using the surface routine in GMT (Smith & Wessel, 1990; Wessel et al., 2019) with tension set to 0.9 of observed/modeled isochrons and various isochrons associated with each of the different models. This table corresponds with Figures 1b–1i and 3a–3h, that show the predicted isochron maps associated with each of the models that we explored. Figures S1 and S2 show difference maps defined as observed-model ages for each grid cell explicitly defined by either of the grids. Table 3 includes percent areas of overlap of the two grids, percent area of non-overlap of the observed/kinematic grid with each model, and non-overlap of each model with the observed/kinematic grid. Both correlations and percent error reflect the percentage of non-overlapping areas as ages or differences of age with 0, Here, it is worth noting that correlations are expected to vary both as a function of age and plate. Correlations at young ages are expected to be high because torque-derived rotations that are only approximately correct will correspond with small angle rotations that cannot yield predicted isochrons that are significantly different from the observed ages. Similarly, following approach 1, predicted age distributions on the Pacific plate can at most be different by ~6% difference of the rotation, because of the attempt to minimize differences on the Farallon plate, whereas approach 2 yields a perfect match on the Pacific plate, while forcing all of the misfit onto the Farallon plate. Thus, the differences in correlation coefficients primarily reflects differences on the Farallon plate and at older ages. For this reason, for approach 1 we report correlations of the total area, Pacific, and Farallon plates separately (Table 3), whereas for approach 2 we only focus on the Farallon plate.

As will be noted from Table 3, areas of overlap range from 70% to 87% for approach 1% and 55%–90% for approach 2. Areas of non-overlap with the observed/kinematic grid are generally small (<6%), except for model 3 using approach 2 (11%). Areas of non-overlap with model grids range from 7% to 26% for approach 1%, and 5%–34% for approach 2. Correlation coefficients are, in general, rather low, with values ranging from 0.061 to 0.371 over the entire area for approach 1, and from −0.173 to 0.573 for approach 2. Finally, percent error ranges from 56.8% to 89.5% over the entire area, and 61.4%–120.3% over the Farallon plate based on approach 1. Using approach 2, percent error ranges from 31.8% to 201.9%. Based on Table 3 none of the models yield what would be generally considered a good fit to the data. The best fit is provided by model 4 and approach 2. Model 4 and approach 1 also yield the best fit as judged by percent error, while model 7 yields higher correlation for approach 1, and second highest with approach 2. Models 1–3, 5, 6, and 8 all yield negative correlation coefficients for approach 2 and generally high percent errors.

The different models yield different predicted age distributions and therefore fits to observed ages in the Peru-Chile trench, correlations, and percent error, as summarized in Tables 2 and 3. Models 2 through 8 are characterized by a relatively sharp southward deviation between ages 15 and 30 Ma or 40 Ma, which is particularly pronounced with models 3–7, using both approaches 1 and 2. There is no deviation in the kinematic reconstruction of Farallon/Nazca isochrons. In addition, despite scaling D in models 1 through 7 to match recent plate motions, models 1–3, and 5–8 using approach 1, and 1, 2, 5–8 using approach 2, are all characterized by significantly greater ridge production, that is greater eastward extent of isochrons than shown in Figure 1a, and thus yield unsatisfactory fits to our base data. This is also highlighted in Table 2 by noting the typically >5 Ma age difference between the observed oldest age in Peru-Chile trench.

Only two models, 4 and to a lesser degree 7, yield better fits to the observed/kinematic age distribution data. First is model 4, which yields the best fit using approach 2, judged by both R and percent error. This model differentially adjusts most of the free parameters to achieve this fit as shown in Table 1. Farallon is scaled by 0.75 $\vec{\tau_S}$ and Pacific by 0.25 $\vec{\tau_S}$, with an intermediate 1.0 $\vec{\tau_T}$,and with independent scaling of D beneath the Farallon and Pacific plates that differ by an order of magnitude, resulting in an order of magnitude difference in implied h and η_a. The difference in $\vec{\tau_S}$ between the Farallon and Pacific plates could be justified by the difference in average age of the currently subducting lithosphere (Tables A1 and A2) that largely pertains from the present to about 50 Ma. Older, thicker lithosphere imposes greater resistance through plate bending (Buffett & Rowley, 2006;

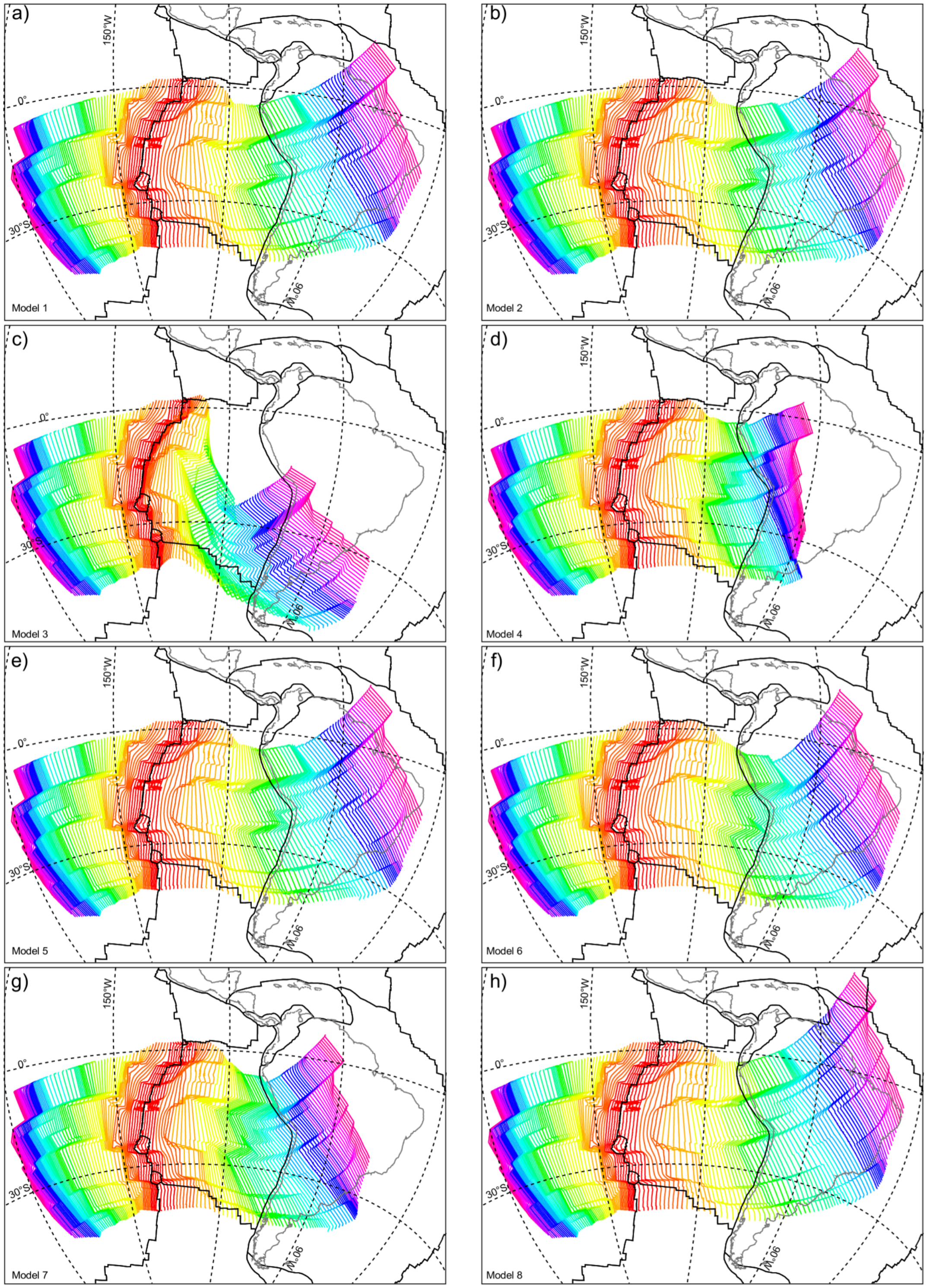

Figure 3. Lambert equal area projections of synthetic Farallon isochrons based on approach 2 for each of the eight torque-derived rotation models.

Conrad & Hager, 1999). However, counter to this is that most western Pacific subduction zones are characterized by significantly steeper slab dips (Syracuse & Abers, 2006), and back-arc spreading, thought to be associated with slab retreat. In contrast, Farallon slab is characterized by a shallow dip (Syracuse & Abers, 2006) associated strong upper plate shortening in the Andes, assumed to be associated with a strongly advancing subduction zone.

Similarly, model 7, imposes differential slab pull on the Farallon and Pacific plates, this time with Pacific greater than Farallon by 045 $\vec{\tau_S}$ versus 0.25 $\vec{\tau_S}$, respectively. In addition, D is also scaled differently, with Farallon about a factor of 2 lower than the Pacific plate resulting in almost a factor of 2 difference in implied h and η_a. As will be highlighted below, when we discuss predicted motion of the EPR as a function of time, models 4 and 7 employ values of D, that are optimized to match observations, but yield unphysical results, where the depth of deformation below the large-aspect ratio Pacific plate is nearly one half that of the much smaller Nazca plate (Model 7) or a factor of >10 different for model 1. We are unaware of any data that support such large contrasts in the depth of the deforming layer.

The primary differences shown in Figures 1 and 3 are in the geometry of synthetic isochrons older than 45 Ma on the Farallon plate. Based on the reconstructions of Rowan and Rowley (2014), the Euler poles relative to the Farallon plate for ages older than 45 Ma are located relatively close to the southern end of these isochrons. This gives rise to the relatively tight concave southward curvature of the major fracture zone just south of the Equator and close spacing of isochrons southwards from there. In marked contrast to this, and for the same interval, all of model-derived rotations, except model 4, retrodict Euler poles relative to the Farallon plate that are ~70° away and to the north giving rise to concave northward curvature of the same fracture zone and approximately equal spacing of synthetic isochrons. The overall configuration of the isochrons in model 4 does the best job visually of matching the observed/modeled isochrons on the Farallon plate, particularly at ages greater than 45 Ma. Older isochrons on the Farallon plate do not reconstruct far enough to the east, but otherwise compare pretty well. However, as discussed above, this fit is achieved through extreme variability of the physical input parameters (Table 1), in particular the drag coefficient D, which implies order of magnitude differences in 'h' from 109 versus 1,333 km, and viscosities of 6.6×10^{20} $\boldsymbol{Pa}$ $\boldsymbol{s}$ to 0.54×10^{20} $\boldsymbol{Pa}$ $\boldsymbol{s}$, under the Farallon and Pacific, respectively. These results demonstrate that although it is possible to match some aspect of the evolution of EPR spreading, given uncertainties in scaling of the various parameters, we have no physical rational that would account for such choices that fall well outside generally accepted limits.

In summary, the results shown in Figures 1 and 3, and summarized in Tables 2 and 3, indicate that none of the models yield satisfactory fits to the observed/kinematic model for the evolution of spreading along the EPR between the Galapagos and Easter triple junctions. Efforts to optimize the match to the observed age distribution, for the best-fitting model 4, requires individually tailored D's and τ_S associated with the Pacific and Farallon plates for which we have no independent physical justification. As expected, given enough independent tunable parameters, it is generally possible to find a combination that yields a reasonable fit.

A second important aspect of the evolution of this region is the effectively longitude parallel trajectory of the EPR axial location as a function of time retrodicted by global plate kinematics in the NNR frame of reference (Rowley et al., 2016). In Figures 4 and 5 we compare the motion of the EPR retrodicted by circum-Pacific torques. For the purposes of illustration, we generate a map of retrodicted positions of the EPR at 5 MY intervals from the Present back to 80 Ma based on our torque calculations using approach 1 (Figure 4) and 2 (Figure 5). Here we note that the majority of the torque-derived models retrodict a west to east migration of the EPR with time. The smallest component of west to east motion of the EPR results from models 4 and 8, using both approaches for reconstructing synthetic isochrons. As discussed above, and in Table 1, model 4 partitions slab pull fractions significantly between the Farallon (75%) and Pacific (25%) and adjusts D's differently under the different plates. We view this model as one attempt to find model parameters that both mimic the isochron evolution and the trajectory of the EPR as a function of time. We did not attempt to further optimize the fit to both of these components because the achieved fit was close enough to provide insight into how substantial the perturbations to the standard slab-pull model needed to be.

Model 8 also does a remarkably good job of retrodicting an absence of longitudinal motion of the EPR. This model partitions slab pull equally to Farallon and Pacific at 50% and uses a priori geodynamic constraints for D, which is the same under both the Farallon and Pacific plates. However, as made clear in Figure 1i, and Table 3, this model yields a poor fit of the predicted isochrons, particularly on the Farallon plate as reflected in $R = 0.074$ and percent error >60% over the total and Farallon areas.

Based on global kinematics, the EPR is retrodicted to have migrated northward, effectively along the same longitude with time. Our global kinematic reconstruction in the NNR frame of reference only extends back to 45 Ma. We can extend the analysis back to 80 Ma as shown in Figure 4b using global kinematic reconstructions in the

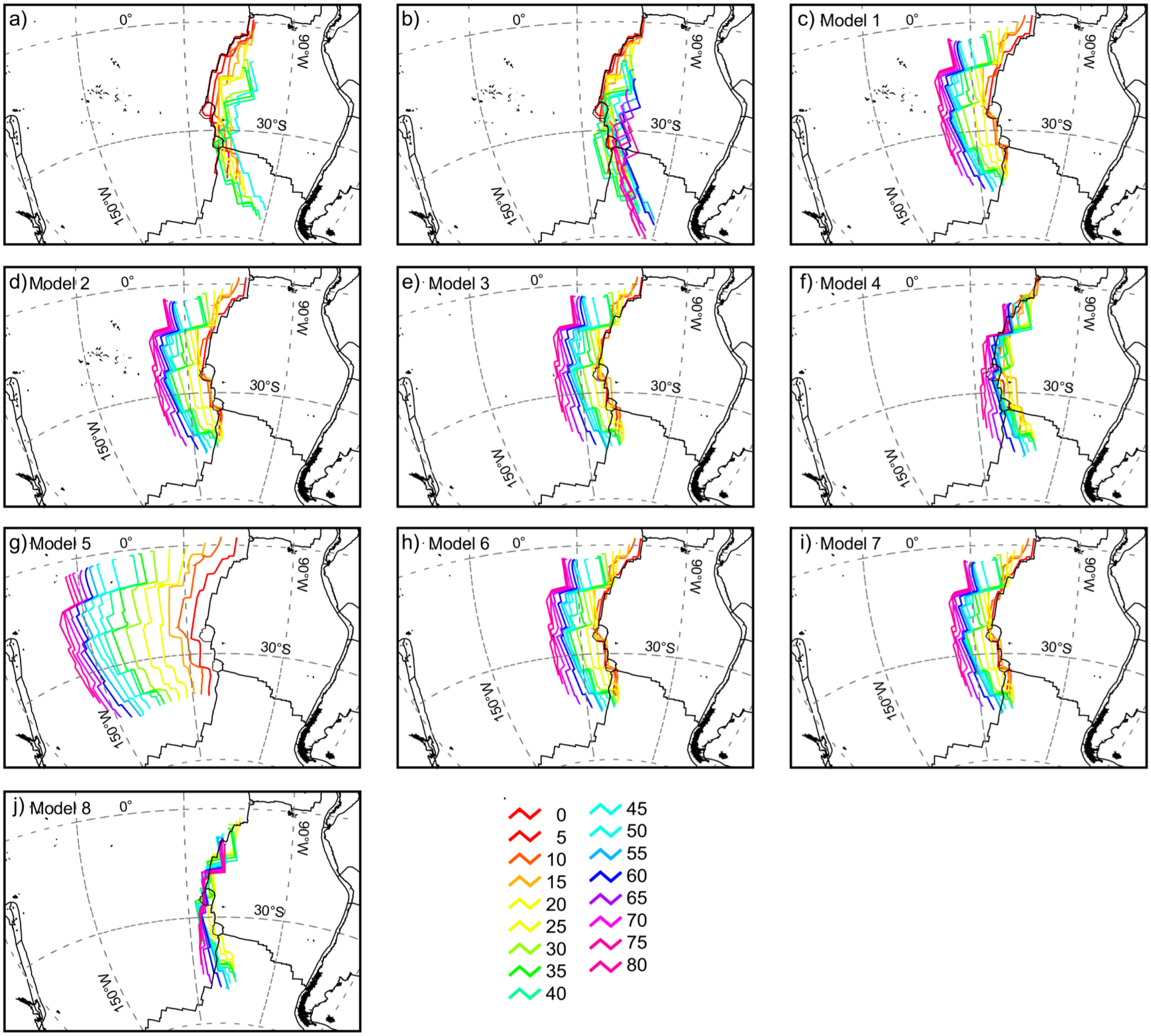

Figure 4. Comparison of the reconstructed position of the EPR in the NNR frame of reference as a function of time based on various reconstructions. (a) EPR relative to NNR back to 45 Ma and (b) EPR relative to fixed Indo-Atlantic hotspot reference frame to 80 Ma from Rowley et al. (2016). (c) through (j) Reconstructions of EPR relative to NNR based approach 1 and the eight models explored in this paper. See Table 1 for the configuration of various parameters of each model.

fixed Indo-Atlantic hotspot frame of O'Neill et al. (2005) that was used by Rowley et al. (2016). The first order kinematics of the EPR in the NNR and Indo-Atlantic frames of reference are not significantly different. Both are characterized by an overall northward migration of the EPR. Thus, the majority of the torque-derived retrodicted motions of the EPR are effectively orthogonal to the motion derived from global kinematics.

The first order observation derived from Figures 1 and 3–5 is that the majority of traditional plate driving force-related retrodicted histories of the EPR are characterized by progressive eastward migration relative to the current EPR since 80 Ma. Obviously, the different models retrodict different magnitudes of eastwards migration ranging from ~5,800 km (model 5) to as low as a few 100 km of westward motion (models 4 and 8) since 80 Ma. Over the past 40 Ma, global plate kinematic reconstructions require 0 km of net eastward motion of the EPR axis (Rowley et al., 2016). Slab-pull would, in general, result in effectively due eastward motion since 80 Ma, whereas global reconstructions yield effectively due northward motions, orthogonal to each other.

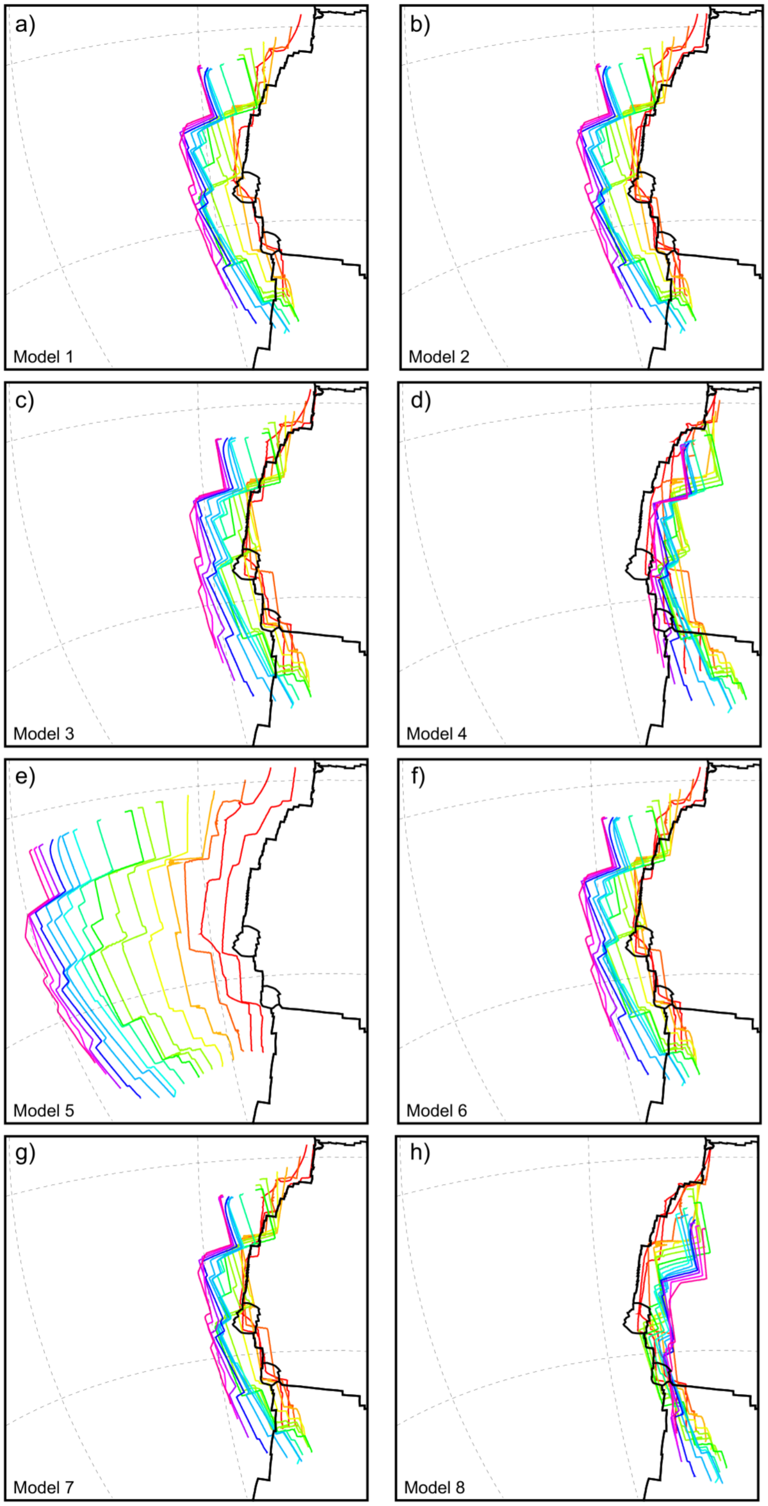

Figure 5. (a) through (h) Reconstructions of EPR relative to NNR, based on approach 2 and the eight models explored in this paper. See Figure 4 for the correlation of color with isochron age.

The major discrepancies between the plate kinematic reconstruction of the motions of the Pacific and Farallon plates in the fixed Indo-Atlantic and Pacific hotspot and NNR frames of reference (Rowley et al., 2016) with those predicted from the reconstructed histories of plate torques, raise important questions regarding plate driving forces. First, Figures 1 and 3 show that there is generally poor resemblance between the ages of oceanic lithosphere of Farallon plate and modeled from kinematics derived from slab-pull and associated resistive torques. There are large misfits as judged by both low spatial correlations and high percent errors of typically >60% over the entire region and even higher when the analysis is restricted to the Farallon plate (Table 3). Second, if the EPR is assumed a passive ridge, there is no explanation for the observed spreading asymmetry (Figure 1a) over at least the last 51 Ma, characterized by ∼44% accretion on the Pacific and ∼56% on average accretion on the Farallon plate (Rowan & Rowley, 2014). Third, as shown by the comparisons in Figures 4a and 4b, most of the torque-derived models yield reconstructed motions of the EPR that are effectively orthogonal and hence incompatible to the observed kinematics, independent of the chosen reference frame. It is possible to more closely match the age distribution and EPR kinematics, as exemplified by model 4, but this requires inclusion of unphysical variability in the drag coefficient D.

4. Discussion

Both Pacific and Farallon plates are effectively bounded by N-S striking trenches over time. As a result, the associated slab-pull torques are reasonably expected to be located close to the north and south poles, respectively. Thus it would be difficult to account for the effectively S to N migration of the EPR along a line of longitude demonstrated by Rowley et al. (2016), irrespective of the distribution of subducting ages along the trenches. Indeed, none of the slab-pull models yields this large-scale northward migration of the EPR. This, in turn, implies that uncertainties in the reconstructions of the paleo-age grids are not likely to provide an explanation, even though there are undoubtedly large uncertainties in both the locations of trenches and the paleo-age grids (Rowley, 2008, 2018). It is also important to note that the disparities between slab-pull predicted and global plate reconstruction derived motions of the EPR persist at all ages, including the most recent intervals where the uncertainties in the paleo-age grids and paleo-plate boundaries are expected to be increasingly smaller. Finally, the consistency among the ridge residence time maps in the Indo-Atlantic, Pacific and NNR frames of reference (Rowley et al., 2016) suggests that the discrepancy is unlikely to arise from uncertainties in the reconstructed motions of the EPR.

Because the discrepancy between the EPR motions retrodicted by slab-pull torques are nearly orthogonal to those from reconstructed global plate kinematics, it is also unlikely that a spatially varying drag coefficient under the plates could play a role. To test this possibility, we carried out simulations in which the drag coefficients under each plate differ, by as much as an order of magnitude, in an effort to maximize the fit between the predicted and observed plate motions models 4 and 7. As expected the main impact of a heterogeneous D coefficient is to amplify or dampen plate rotations, not to cause the rotation axes to change their positions by approximately 90°. Moreover, local variability in D associated with lateral variations in asthenospheric viscosity below the Pacific Ocean, as predicted by mineral physical models (e.g., Glišović et al., 2015), is less than the largest plate-averaged variations we explored.

The modeling and analysis above supports the assessment of Rowley et al. (2016) that there are significant discrepancies between retrodictions based on Pacific and Farallon slab-pull dominated plate motions and those reconstructed from global plate reconstructions. Rowley et al. (2016) used tomography-based global flow models to demonstrate that the EPR is not a passive mid-oceanic ridge, but has instead been coupled over the past 80 Ma or more to a source of deep-mantle derived buoyancy that is a significant driver of Pacific and Farallon plate motions (see also Glišović & Forte, 2014). Thus, rather than asthenospheric drag inhibiting plate motions, the asthenosphere is coupled to and provides basal tractions to the plates that contribute to driving their motions (see also Ghosh & Holt, 2012).

These earlier findings have been further reinforced by the most recent joint tomography inversions by Lu et al. (2020) in which a greatly enlarged suite of global seismic and geodynamic data have been simultaneously inverted to provide greater resolution of the buoyancy distribution in the mantle. The (Lu et al., 2020) inversions tested a number of different viscosity models derived in past independent studies and in all cases strong positive mantle buoyancy is resolved below the EPR, which drives a mantle-wide upwelling centered below this ridge. We can explicitly demonstrate the geodynamic importance of this deep-seated positive buoyancy by determining the predicted plate motions in the Pacific Ocean for three cases: (a) the entire mantle-wide distribution of density anomalies is employed to predict the flow; (b) the flow is predicted by removing all positive buoyancy below the

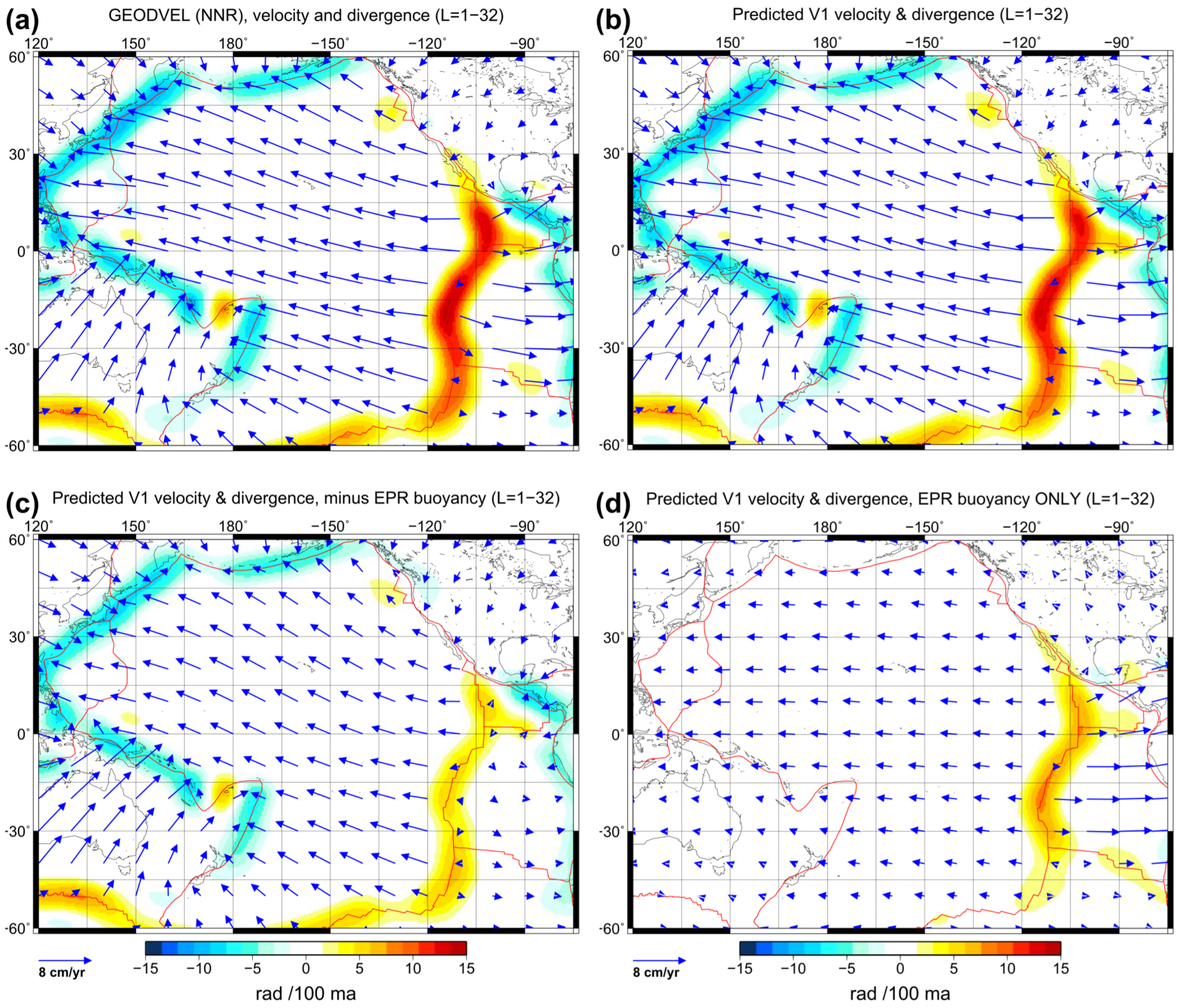

Figure 6. Observed and predicted present-day plate motions in the no-net-rotation (NNR) reference frame. Blue arrows represent the horizontal velocity and the colors represent the rate of horizontal divergence of the plates, where both are measured relative to the amplitude scales at bottom of the figure. (a) The observed plate motions given by the GEODVEL model (Argus et al., 2010). (b) The plate motions predicted by a mantle flow calculation using the "V1 model" of density anomalies derived from joint seismic-geodynamic inversions (Lu et al., 2020). (c) The plate motions predicted by the V1 model (as in b), except that all positive buoyancy below the EPR, for all depths greater than 400 km, is not included. (d) The plate motions predicted only with the deep positive buoyancy below the EPR (i.e., the complement of c). In all cases, the surface motions are represented by a spherical harmonic expansion that is truncated at degree $\ell = 32$.

EPR, for all depths greater than 400 km; and (c) mantle flow and overlying plate motions are driven only by the positive buoyancy below the EPR, at all depths greater than 400 km. The mantle density anomalies employed in each of these cases were obtained from a joint tomography inversions, denoted the "V1 model" (for details see Lu et al., 2020), which employed the radial viscosity profile derived from simultaneous inversion of GIA and mantle convection data sets (Mitrovica & Forte, 2004).

The surface plate motions predicted for each of these three cases are compared with the observations in Figure 6. The predicted flow that integrates all mantle density anomalies, shown in Figure 6b, provides an excellent match to the observed present-day velocities (Figure 6a), characterized by a global root-mean-square (rms) velocity difference of only 0.25 cm/yr relative to the observed global rms velocity of 4.38 cm/yr in a no-net-rotation (NNR) reference frame. The observed rms velocity of the Pacific and Nazca plates (Figure 6a), in the NNR frame, are both equal to 6.6 cm/yr whereas the corresponding predicted rms velocities (Figure 6b) are both 6.3 cm/yr, again confirming the excellent fit provided by the mantle flow calculation based on the V1 tomography model. Figure 6c shows the predicted plate motions, when all positive buoyancy below the EPR is removed for all depths greater than 400 km. In this case, the rms velocities of the Pacific and Nazca plates are of 4.1 and 1.5 cm/yr, respectively, corresponding to reductions of 35% and 76%, respectively, relative to the plate motions predicted in Figure 6b.

A quantification of the importance of the plate driving forces arising from the hot mantle upwelling deep below the EPR is further illustrated in Figure 6d, which shows the predicted plate motions driven entirely by the deep positive buoyancy in all depths greater than 400 km below the EPR. In this last case, the rms velocity of the Pacific and Nazca plates are 2.4 and 5.1 cm/yr, respectively, which are 38% and 81% of the rms velocities predicted with all buoyancy in the mantle (Figure 6b). The rms velocity of the plate motions, integrated over the entire region shown in Figure 6b, is 2 cm/yr, which is 46% of the rms plate velocities in Figure 6b. Another important aspect shown in Figure 6d is the asymmetry in the flow beneath the Pacific and Nazca plates. This was extensively discussed in Rowley et al. (2016) both for the present and past geodynamic reconstructions, and provides an explanation for the persistent asymmetric spreading along the EPR that can not be accounted for by passive upwelling into the gap generated by far-field plate-related driving forces.

Finally, we find that the torque due to the basal tractions on the Pacific and Nazca plates exerted by deep positive buoyancy below the EPR (Figure 3d) are $6.0 \times 10^{26}\ \mathrm{N\ m}$ and $2.0 \times 10^{26}\ \mathrm{N\ m}$, respectively. To appreciate these magnitudes, we note that torques generated by the net slab-pull forces (reduced to 25% of their weight, due to mantle and lithospheric dissipation at the subduction zones, not including the collision resistance force of the overriding plates) are $5.2 \times 10^{26}\ \mathrm{N\ m}$ and $1.6 \times 10^{26}\ \mathrm{N\ m}$ for the Pacific and Nazca plates respectively. It is thus clear that basal tractions generated by positive buoyancy in the upwelling mantle below the EPR are just as important as slab pull in driving plate motions in the Pacific Ocean.

5. Implications

It has long been argued that slab-pull is the dominant force driving plate tectonics (Coltice et al., 2019; Conrad & Lithgow-Bertelloni, 2004; Elsasser, 1969; Forsyth & Uyeda, 1975; Richter, 1973b, 1977). Perhaps the most seminal work that underlies this longstanding view that slab-pull dominates derives from Richter (1973a, 1977), Richter and Parsons (1975) in which it was demonstrated that small-scale convection in the sublithospheric upper mantle will be characterized by rolls, often referred to as Richter Rolls (Korenaga, 2003). These rolls are elongated in the direction of plate motion, with flow around the rolls in a direction perpendicular to plate motion. Obviously, such flows cannot drive plate motions and therefore a general view has emerged (with notable exceptions discussed above) that basal tractions generated by the mantle-wide convective circulation are not important plate driving forces.

What is often ignored is that when the scale of the large-scale convection is comparable to the length scale of the plates themselves, then Richter Rolls do not form. In the geodynamic models of Forte et al. (2010), Ghosh and Holt (2012), Glišović and Forte (2014) the convective flows driving plate motions derived from integrating all sources of buoyancy are mantle wide. In the specific case of the EPR, the radial extent of the flow is from the CMB to the surface (Glišović & Forte, 2014; Rowley et al., 2016), and hence the depth scale and horizontal scale are comparable, leading to the suppression of Richter Rolls. Thus the arguments against active mantle tractions, as put forth in these classic treatments of plate driving forces (Forsyth & Uyeda, 1975; Richter, 1973a; Solomon & Sleep, 1974), need to be reconsidered in light of significant changes in our assessment of the geometry of mantle convection and significant core-mantle boundary contributions to the deep mantle buoyancy flux and global heat flux at the top of mantle (Glišović & Forte, 2014, 2017; Rowley et al., 2016).

6. Conclusions

We use published paleo-age grids (Müller et al., 2008) and corresponding paleo-plate boundary polygons (Gurnis et al., 2012) to derive estimates of the slab-pull torques operating on the Pacific and Farallon plates as a function of time since 80 Ma. When balanced with resistive forces arising from mantle drag and those acting along plate-boundaries, we derive estimates of the Pacific and Farallon rotations relative to the NNR as a function a time over this same interval. We compare the retrodicted motions of the plates and particularly the EPR derived from this analysis with those based on global plate reconstructions. This comparison demonstrates significant discrepancies between these reconstructions in term of: (a) predicted spreading histories and corresponding age distributions adjacent to the EPR; and (b) S to N motion of the EPR relative to the underlying mantle as derived by global plate reconstructions, and essentially orthogonal, eastward motion of the EPR retrodicted by balancing slab-pull derived torques.

These discrepancies provide additional support for the interpretation that deep-mantle derived buoyancy driven flow beneath the EPR is contributing to and potentially controlling the behavior of the EPR. As demonstrated here, the resulting advective motions within the asthenosphere significantly contribute to plate motions, at least in the Pacific region. This conclusion is strongly supported by recent tomography-based mantle flow modeling (Figure 6). The work and analysis presented above contributes to arguments that deep mantle buoyancy, along with slab-pull related negative buoyancy, jointly provide the primary contributors to plate motions.

Appendix A

The torque due to the slab-pull, $d\,\vec{\tau}_S$, acting on a particular trench segment of length dl is

$$d\,\vec{\tau}_S = \vec{r}\times(F_S dl)\hat{n} \tag{A1}$$

where $F_S(t)$ is the slab pull force per unit length, given by expression (1) in the main text, and $\hat{n}$ is a unit vector perpendicular to the strike of the trench. We note that

$$\hat{l}\times\hat{r}=\hat{n} \tag{A2}$$

and where the unit vector $\hat{l}$ points along the trench, in a counter-clockwise direction (relative to the plate interior) around the subducting plate. Combining (A1) and (A2), yields:

$$d\,\vec{\tau}_S = \vec{r}\times(\vec{dl}\times\hat{r})F_S = (r_0 F_S)\ \hat{r}\times(\vec{dl}\times\hat{r}) \tag{A3}$$

where $\vec{dl} = (dl)\hat{l}$ and r_0 is the radius of Earth's solid surface.

Integrating (A3) counterclockwise around the perimeter of the subducting plate yields the total torque due to the slab-pull force:

$$\vec{\tau}_S = r_0 \int F_S(t)\hat{r}\times(\vec{dl}\times\hat{r})$$

that can be rewritten as

$$\vec{\tau}_S = r_0 \int F_S(t)[(\hat{r}\cdot\hat{r})\,\vec{dl} - (\hat{r}\cdot\vec{dl})\hat{r}]$$

that in turn simplifies to:

$$\vec{\tau}_S = r_0 \int F_S(t)\,\vec{dl} \tag{A4}$$

because $(\hat{r}\cdot\hat{r}) = 1$ and $(\hat{r}\cdot\vec{dl}) = 0$, and the line integral in (A4) is counterclockwise around the subducting plate boundary.

Expression (A4) is numerically evaluated by assuming that the age of the subducting plate is approximately constant over small, but finite segments of the trench:

$$\vec{\tau}_S \cong r_0 \sum_{i=1}^{N} F_S(t_i) \int_{\vec{r}_{i-1}}^{\vec{r}_i} \vec{dl} = r_0 \sum_{i=1}^{N} F_S(t_i)\,\vec{\Delta l}_i \tag{A5}$$

where $\vec{\Delta l}_i = \vec{r}_i - \vec{r}_{i-1}$ is the vector difference of the position of the end points of each trench segment in which the age is assumed to be constant. To recap, in expression (A5), the starting and end points of each trench segment, on which the plate age $t = t_i$ ($i = 1$, N) may be assumed approximately constant, are $\vec{r}_{i-1}$ and $\vec{r}_i$, respectively. The sum in (A5) must proceed in a counterclockwise direction along the trench.

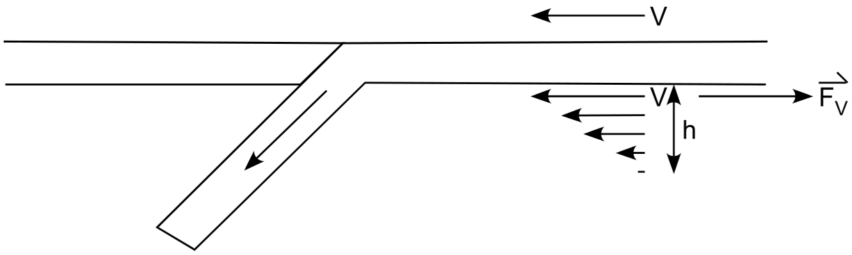

Figure A1. Schematic representation of the viscous tractions resisting the slab-pull force.

The slab-pull torque (A4) will drive a rotational motion of the plate that will be opposed by resistive forces acting on the bounding edges of the plate and by drag-related viscous forces acting on the base of the plate, as indicated in Equation 7 in the main text.

The following schematic (Figure A1) will help explain the derivation of the viscous drag opposing the subduction-related torque. The model assumes that the force exerted by the plate on the underlying mantle is due to Couette flow, which may be thought of as simple shear relative to a presumed passive and stagnant deeper mantle (Figure A1). That force is

$$\vec{F} = \eta \frac{\Delta \vec{V}}{\Delta Z} \ (z \text{ is depth}) = \ \eta \frac{\vec{V}}{h} = D\,\vec{V}, \ \text{ where } \ = \frac{\eta}{h}. \tag{A6}$$

Therefore, the viscous drag force (per unit area) of the mantle opposing the motion of the overlying plate is:

$$\vec{F_V} = -D\,\vec{V}, \tag{A7}$$

where $\vec{F_V}$ acts on all areas at the base of the plate. The drag coefficient, $\boldsymbol{D}$, defined in (A6), could be spatially variable, due for example to lateral viscosity variations, and $\boldsymbol{h}$ is here assumed to be the depth of the "base" of the asthenosphere (Figure A1).

The velocities of effectively rigid plates constrained to move on a spherical surface may be represented, according to Euler's theorem, in terms of rigid-body rotations

$$\vec{V} = \vec{\omega} \ \times \ \vec{r}, \tag{A8}$$

where $\vec{\omega}$ is the angular velocity of the plate. We can thus rewrite (A7) as:

$$\vec{F_V} = -D(\vec{\omega} \ \times \ \vec{r})$$

and the total drag-related torque acting on the base of the plate of area A is

$$\begin{aligned}
\vec{\tau_V} &= \iint_A \vec{r} \ \times \ F_V\, dA = \ -\iint_A D \ \ \vec{r} \times (\vec{\omega} \ \times \ \vec{r})\, dA \\
&= -D \iint_A \ [(\vec{r} \cdot \ \vec{r})\, \vec{\omega} - (\vec{r} \cdot \vec{\omega}) \ \vec{r} \ ]\, dA \\
&= -D \iint_A \ [{r_0}^2 \ \vec{\omega} - (x_i \hat{e}_i)(x_j \omega_j) \ ]\, dA \\
&= -D \left[A{r_0}^2 \ \vec{\omega} - \hat{e}_i \left(\iint_A x_i x_j\, dA \right) \ \omega_j \right] \\
&= -D[A{r_0}^2 \hat{e}_i \delta_{ij} \omega_j - \hat{e}_i S_{ij} \omega_j]
\end{aligned}$$

Hence,

$$\vec{\tau}_V = -D{r_0}^2 A\hat{e}_i[\delta_{ij} - \widehat{S_{ij}}]\omega_j, \quad \text{where } \widehat{S_{ij}} = \frac{1}{r_0^2 A}\iint\limits_A x_i x_j \, dA \ , \tag{A9}$$

where $\hat{e}_i$ are the unit direction vectors in a Cartesian coordinate system whose origin is at Earth's center of mass and $\delta_{ij}(=\hat{e}_i \cdot \hat{e}_j)$ is the Kronecker delta. We assume here that D is constant under each plate. The use of a globally constant (i.e., spatially uniform) value of the drag coefficient D yields plate motions in a no-net-rotation (NNR) mantle frame of reference (Solomon & Sleep, 1974). From a numerical perspective, it is interesting to note the symmetric matrix $\hat{S}_{ij}$ has diagonally dominant terms, whose trace is identically equal to one. Expression (A9) thus implies an approximate parallelism between the total torque vector acting on a plate and its resulting angular velocity vector.

In addition to basal drag, we explored the importance of resistive forces acting on the bounding edges or sides of the plates. The two principal edge forces we modeled are the frictional forces acting tangentially (along the face) of transform (strike-slip) boundaries and collisional resistance forces acting on the subducting edges of the plates. Following Becker and O'Connell (2001), we model the torques due to these resistive edge forces as follows:

$$\text{(transform resistance)} \quad \vec{\tau}_T = -C_T \ r_0 \int\limits_{TF} sgn(v_t) \ \hat{r} \times \hat{l} \ dl, \tag{A10}$$

$$\text{(collision resistance)} \quad \vec{\tau}_C = -C_C \ r_0 \int\limits_{CR} \hat{r} \times \hat{n} \ dl, \tag{A11}$$

where the orientations of the unit vectors $\hat{r}$, $\hat{n}$, $\hat{l}$ are defined as before (see A2). The function $sgn(v_t) = 1$ or -1, depending on the orientation of the tangential relative velocity, v_t, with respect to the tangent vector $\hat{l}$. (If the plate edge is not a transform boundary, $sgn(v_t) = 0$) All line integrals are counterclockwise relative to the plate interior and only include segments that are either transform boundaries (in A10) or subduction boundaries (in A11). The factors C_T and C_C determine the local magnitude or strength of the transform and collision resistance forces, respectively, and they are assumed to be constant in value (Becker & O'Connell, 2001). On the basis of expression (A2), and the derivation leading to (A4), we may further simplify expressions (A10) and (A11) as follows:

$$\vec{\tau}_T = C_T \ r_0 \int\limits_{TF} sgn(v_t) \ \hat{n} \ dl, \tag{A12}$$

$$\vec{\tau}_C = -C_C \ r_0 \int\limits_{CR} \vec{dl} = -C_C \ r_0 \ \ \vec{\Delta l}, \tag{A13}$$

where $\vec{\Delta l} = \vec{r_1} - \vec{r}_0$ is the vector difference of the position at the start and end points of the subduction boundary segment, along which the collision resistance force is assumed constant.

The very high viscosity of the mantle implies an effectively infinite Prandtl number and hence inertial forces are completely negligible. This implies that the sum of all forces and associated torques must equal to zero everywhere in the mantle. It then follows that the sum of all torques acting on a tectonic plate must also balance to zero, such that:

$$\vec{\tau}_S + \vec{\tau}_T + \vec{\tau}_C + \vec{\tau}_V = 0. \tag{A14}$$

In the presence of active basal tractions produced by buoyancy-induced viscous mantle flow, expression (A14) must also include the torque exerted on each plate, $\vec{\tau}_M$, due to these additional basal tractions:

$$\vec{\tau}_S + \vec{\tau}_M + \vec{\tau}_T + \vec{\tau}_C + \vec{\tau}_V = 0.$$

In the analysis presented in the main text, we focus on the hypothesis that slab-pull torques are the primary drivers of observed plate motions, and their changes with time, and hence we work with expression (A14).

If we now substitute all torques given by expressions (A4), (A9), (A12) and (A13) into the torque balance Equation A14, we obtain:

$$r_0 \int F_S(t)\, \vec{dl} + C_T\ r_0 \int_{TF} sgn(v_t)\ \hat{n}\ dl - C_C\ r_0 \int_{CR} \vec{dl} = D{r_0}^2 A \hat{e}_i [\delta_{ij} - \hat{S}_{ij}] \omega_j$$

$$\Leftrightarrow (D r_0 A)^{-1} \hat{e}_i \cdot \left[\int F_S(t)\, \vec{dl} + C_T \int_{TF} sgn(v_t)\ \hat{n}\ dl - C_C \int_{CR} \vec{dl} \right] = [\delta_{ij} - \hat{S}_{ij}] \omega_j. \tag{A15}$$

Expression (A15) may be rewritten as the following linear set of equations that can be inverted to solve for the Cartesian components ω_i of the plate rotation vector:

$$f_i = \sum_{j=1}^{3} A_{ij} \omega_j, \quad (i = \ 1, 2, 3)$$

where

$$f_i = \ (D r_0 A)^{-1} \hat{e}_i \cdot \left[\int F_S(t)\, \vec{dl} + C_T \int_{TF} sgn(v_t)\ \hat{n}\ dl - C_C \int_{CR} \vec{dl} \right] \text{ and } A_{ij} = \ [\delta_{ij} - \hat{S}_{ij}],$$

which finally yields

$$\omega_i = \ \sum_{j=1}^{3} {A_{ij}}^{-1} f_j. \tag{A16}$$

Data Availability Statement

All data used are publicly available at urls that were provided with the submission.

Acknowledgments
DBR and AMF thank colleagues of the former ESEP-CIFAR group for discussions. DBR thanks Petar Glisovic for assistance in organizing paleo-age grid and plate-boundary polygon files. DBR acknowledges contributors to the Rowley Research Funds and Paleogeographic Atlas Project at The University of Chicago for their generous support. AMF acknowledges support of this work provided by NSF grant EAR-1903108 as well as by the University of Florida. AMF also acknowledges support from the French “Programme d'investissements d'avenir” under the auspices of the GYPTIS project – ANR 19 MPGA 0007.

References

Argus, D. F., Gordon, R. G., Heflin, M. B., Ma, C., Eanes, R. J., Willis, P., et al. (2010). The angular velocities of the plates and the velocity of Earth's centre from space geodesy. *Geophysical Journal International*, *180*(3). 913–960. https://doi.org/10.1111/j.1365-246X.2009.04463.x

Barckhausen, U., Ranero, C. R., Cande, S. C., Engels, M., & Weinrebe, W. (2008). Birth of an intraoceanic spreading center. *Geology*, *36*(10), 767. https://doi.org/10.1130/G25056A.1

Becker, T. W., & O'Connell, R. J. (2001). Predicting plate velocities with mantle circulation models. *Geochemistry, Geophysics, Geosystems*, *2*(12). https://doi.org/10.1029/2001GC000171

Bird, P. (1999). Thin-plate and thin-shell finite-element programs for forward dynamic modeling of plate deformation and faulting1Code. *Computers & Geosciences*, *25*(4), 383–394. https://doi.org/10.1016/S0098-3004(98)00142-3

Bird, P. (2003). An updated digital model of plate boundaries. *Geochemistry, Geophysics, Geosystems*, *4*, 52. https://doi.org/10.1029/2001GC000252

Bird, P., Liu, Z., & Rucker, W. K. (2008). Stresses that drive the plates from below: Definitions, computational path, model optimization, and error analysis. *Journal of Geophysical Research*, *113*, 32. https://doi.org/10.1029/2007JB005460

Buffett, B., & Rowley, D. (2006). Plate bending at subduction zones: Consequences for the direction of plate motions. *Earth and Planetary Science Letters*, *245*, 359–364. https://doi.org/10.1016/j.epsl.2006.03.011

Cande, S. C., & Haxby, W. F. (1991). Eocene propagating rifts in the southwest Pacific and their conjugate features on the Nazca plate. *Journal of Geophysical Research*, *96*(B12), 19609–19622. https://doi.org/10.1029/91jb01991

Coltice, N., Husson, L., Faccenna, C., & Arnould, M. (2019). What drives tectonic plates? *Science Advances*, *5*(10), eaax4295. https://doi.org/10.1126/sciadv.aax4295

Conrad, C. P., & Hager, B. H. (1999). Effects of plate bending and fault strength at subduction zones on plate dynamics. *Journal of Geophysical Research*, *104*(B8), 17551–17571. https://doi.org/10.1029/1999jb900149

Conrad, C. P., & Lithgow-Bertelloni, C. (2004). The temporal evolution of plate driving forces: Importance of “slab suction” versus “slab pull” during the Cenozoic. *Journal of Geophysical Research*, *109*. https://doi.org/10.1029/2004JB002991

Croon, M. B., Cande, S. C., & Stock, J. M. (2008). Revised Pacific-Antarctic plate motions and geophysics of the Menard Fracture Zone. *Geochemistry, Geophysics, Geosystems*, *9*, Q07001. https://doi.org/10.1029/2008GC002019

de Koker, N., Steinle-Neumann, G., & Vlcek, V. (2012). Electrical resistivity and thermal conductivity of liquid Fe alloys at high P and T, and heat flux in Earth's core. *Proceedings of the National Academy of Sciences*, *109*(11), 4070–4073. https://doi.org/10.1073/pnas.1111841109

Elsasser, W. M. (1969). Convection and stress propagation in the upper mantle. In S. K. Runcorn (Ed.), *The application of modern physics to the Earth and planetary interiors* (pp. 223–246). Wiley-Interscience.

Elsasser, W. M. (1971). Sea-floor spreading as thermal convection. *Journal of Geophysical Research*, *76*(5), 1101–1112. https://doi.org/10.1029/JB076i005p01101

Faccenna, C., Becker, T. W., Lallemand, S., & Steinberger, B. (2012). On the role of slab pull in the Cenozoic motion of the Pacific plate. *Geophysical Research Letters*, *39*. https://doi.org/10.1029/2011gl050155

Forsyth, D., & Uyeda, S. (1975). Relative importance of driving forces of plate motion. *Geophysical Journal of the Royal Astronomical Society*, *43*(1), 163–200. https://doi.org/10.1111/j.1365-246x.1975.tb00631.x

Forte, A. M. (2011). Plate driving forces. In H. K. Gupta (Ed.), *Encyclopedia of Solid Earth Geophysics* (pp. 977–983). Springer. https://doi.org/10.1007/978-90-481-8702-7_215

Forte, A. M., Moucha, R., Rowley, D. B., Quéré, S., Mitrovica, J. X., Simmons, N. A., et al. (2009). Recent tectonic plate decelerations driven by mantle convection. *Geophysical Research Letters*, *36*, 6. https://doi.org/10.1029/2009GL040224

Forte, A. M., Quéré, S., Moucha, R., Simmons, N. A., Grand, S. P., Mitrovica, J. X., & Rowley, D. B. (2010). Joint seismic–geodynamic-mineral physical modelling of African geodynamics: A reconciliation of deep-mantle convection with surface constraints. *Earth and Planetary Science Letters*, *295*(3–4), 329–341. https://doi.org/10.1016/j.epsl.2010.03.017

Ghosh, A., & Holt, W. E. (2012). Plate motions and stresses from global dynamic models. *Science*, *335*, 838–843. https://doi.org/10.1126/science.1214209

Glišović, P., & Forte, A. M. (2014). Reconstructing the Cenozoic evolution of the mantle: Implications for mantle plume dynamics under the Pacific and Indian plates. *Earth and Planetary Science Letters*, *390*, 146–156. https://doi.org/10.1016/j.epsl.2014.01.010

Glišović, P., & Forte, A. (2017). On the deep-mantle origin of the Deccan Traps. *Science*, *355*, 613–616.

Glišović, P., Forte, A. M., & Ammann, M. W. (2015). Variations in grain size and viscosity based on vacancy diffusion in minerals, seismic tomography, and geodynamically inferred mantle rheology. *Geophysical Research Letters*, *42*, 6278–6286. https://doi.org/10.1002/2015gl065142

Glišović, P., Forte, A. M., & Moucha, R. (2012). Time-dependent convection models of mantle thermal structure constrained by seismic tomography and geodynamics: Implications for mantle plume dynamics and CMB heat flux. *Geophysical Journal International*, *190*, 785–815. https://doi.org/10.1111/j.1365-246X.2012.05549.x

Gurnis, M., Turner, M., Zahirovic, S., DiCaprio, L., Spasojevic, S., Müller, R. D., et al. (2012). Plate tectonic reconstructions with continuously closing plates. *Computers & Geosciences*, *38*(1), 35–42. https://doi.org/10.1016/j.cageo.2011.04.014

Hayes, G. P., Moore, G. L., Portner, D. E., Hearne, M., Flamme, H., Furtney, M., & Smoczyk, G. M. (2018). Slab2, a comprehensive subduction zone geometry model. *Science*, *362*(6410), 58–61. https://doi.org/10.1126/science.aat4723

Korenaga, J., & Jordan, T. H. (2003). Linear stability analysis of Richter rolls. *Geophysical Research Letters*, *30*(22). https://doi.org/10.1029/2003gl018337

Lu, C., Forte, A. M., Simmons, N. A., Grand, S. P., Kajan, M. N., Lai, H., & Garnero, E. J. (2020). The sensitivity of joint inversions of seismic and geodynamic data to mantle viscosity. *Geochemistry, Geophysics, Geosystems*, *21*. https://doi.org/10.1029/2019gc008648

Mitrovica, J. X., & Forte, A. M. (2004). A new inference of mantle viscosity based upon joint inversion of convection and glacial isostatic adjustment data. *Earth and Planetary Science Letters*, *225*(1–2), 177–189. https://doi.org/10.1016/j.epsl.2004.06.005

Müller, R. D., Sdrolias, M., Gaina, C., Steinberger, B., & Heine, C. (2008). Long-term sea-level fluctuations driven by ocean basin dynamics. *Science*, *319*(5868), 1357–1362.

O'Neill, C., Müller, R., & Steinberger, B. (2005). On the uncertainties in hot spot reconstructions and the significance of moving hot spot reference. *Geochemistry, Geophysics, Geosystems*, *6*. https://doi.org/10.1029/2004GC000784

Parsons, B., & Richter, F. (1980). A relation between the driving force and geoid anomaly associated with mid-ocean ridges. *Earth and Planetary Science Letters*, *51*(2), 445–450. https://doi.org/10.1016/0012-821x(80)90223-x

Pozzo, M., Davies, C., Gubbins, D., & Alfè, D. (2012). Thermal and electrical conductivity of iron at Earth's core conditions. *Nature*, *485*, 355–358. https://doi.org/10.1038/nature11031

Ricard, Y., & Vigny, C. (1989). Mantle dynamics with induced plate tectonics. *Journal of Geophysical Research*, *94*(B12). https://doi.org/10.1029/JB094iB12p17543

Richter, F. M. (1973a). Convection and the large-scale circulation of the mantle. *Journal of Geophysical Research*, *78*(35), 8735–8745. https://doi.org/10.1029/JB078i035p08735

Richter, F. M. (1973b). Dynamical models for sea floor spreading. *Reviews of Geophysics*, *11*(2), 223–287. https://doi.org/10.1029/rg011i002p00223

Richter, F. M. (1977). Driving mechanism of plate tectonics. *Tectonophysics*, *38*, 61–88. https://doi.org/10.1016/0040-1951(77)90201-3

Richter, F. M., & Parsons, B. (1975). On the interaction of two scales of convection in the mantle. *Journal of Geophysical Research*, *80*, 2529–2541. https://doi.org/10.1029/jb080i017p02529

Rowan, C. J., & Rowley, D. B. (2014). Spreading behaviour of the Pacific-Farallon ridge system since 83 Ma. *Geophysical Journal International*, *197*(3), 1273–1283. https://doi.org/10.1093/gji/ggu056

Rowan, C. J., & Rowley, D. B. (2016). Preserved history of global mean spreading rate: 83 Ma to present. *Geophysical Journal International*, *208*(2), 1173–1183. https://doi.org/10.1093/gji/ggw277

Rowley, D. B. (2008). Extrapolating oceanic age distributions: Lessons from the Pacific Region. *The Journal of Geology*, *116*(6), 587–598. https://doi.org/10.1086/592276

Rowley, D. B. (2018). Oceanic axial depth and age-depth distribution of oceanic lithosphere: Comparison of magnetic anomaly picks versus age-grid models. *Lithosphere*, *11*(1), 21–43. https://doi.org/10.1130/l1027.1

Rowley, D. B., Forte, A. M., Rowan, C. J., Glišović, P., Moucha, R., Grand, S. P., & Simmons, N. A. (2016). Kinematics and dynamics of the East Pacific Rise linked to a stable, deep-mantle upwelling. *Science Advances*, *2*(12). https://doi.org/10.1126/sciadv.1601107

Seton, M., Müller, R. D., Zahirovic, S., Gaina, C., Torsvik, T., Shephard, G., et al. (2012). Global continental and ocean basin reconstructions since 200 Ma. *Earth-Science Reviews*, *113*(3–4), 212–270. https://doi.org/10.1016/j.earscirev.2012.03.002

Smith, W. H. F., & Wessel, P. (1990). Gridding with continuous curvature splines in tension. *Geophysics*, *55*(3), 293–305. https://doi.org/10.1190/1.1442837

Solomon, S. C., & Sleep, N. H. (1974). Some simple physical models for absolute plate motions. *Journal of Geophysical Research*, *79*(17), 2557–2567. https://doi.org/10.1029/JB079i017p02557

Solomon, S. C., Sleep, N. H., & Richardson, R. M. (1975). On the forces driving plate tectonics: Inferences from absolute plate velocities and intraplate stress. *Geophysical Journal of the Royal Astronomical Society*, *42*, 769–801.

Stein, S., Melosh, H., & Minster, J. (1977). Ridge migration and asymmetric sea-floor spreading. *Earth and Planetary Science Letters*, *36*, 51–62. https://doi.org/10.1016/0012-821x(77)90187-x

Stotz, I. L., Iaffaldano, G., & Davies, D. R. (2018). Pressure-driven poiseuille flow: A major component of the torque-balance governing Pacific plate motion. *Geophysical Research Letters*, *45*, 117–125. https://doi.org/10.1002/2017gl075697

Syracuse, E. M., & Abers, G. A. (2006). Global compilation of variations in slab depth beneath arc volcanoes and implications. *Geochemistry, Geophysics, Geosystems*, *7*, Q05017. https://doi.org/10.1029/2005GC001045

Takeuchi, C. S., & Fialko, Y. (2012). Dynamic models of interseismic deformation and stress transfer from plate motion to continental transform faults. *Journal of Geophysical Research*, *117*. https://doi.org/10.1029/2011jb009056

Tebbens, S., & Cande, S. (1997). Southeast Pacific tectonic evolution from early Oligocene to Present. *Journal of Geophysical Research*, *102*(B6), 12061–12084. https://doi.org/10.1029/96jb02582

Torsvik, T. H., Steinberger, B., Shephard, G. E., Doubrovine, P. V., Gaina, C., Domeier, M., et al. (2019). Pacific-Panthalassic reconstructions: Overview, errata and the way forward. *Geochemistry, Geophysics, Geosystems*, *20*(7), 3659–3689. https://doi.org/10.1029/2019gc008402

Turcotte, D. L., & Schubert, G. (2002). *Geodynamics* (2nd Ed.). Cambridge University Press.

Wessel, P., Luis, J. F., Uieda, L., Scharroo, R., Wobbe, F., Smith, W. H. F., & Tian, D. (2019). The generic mapping tools Version 6. *Geochemistry, Geophysics, Geosystems*, *20*, 5556–5564. https://doi.org/10.1029/2019GC008515